A METHOD FOR DRAG REDUCTION ON BLUFF BODIES

by

FRANCOIS LESAGE

B.Sc.A., Université Laval, 1979

A THESIS SUBMITTED IN PARTIAL FULFILMENT OF

THE REQUIREMENTS FOR THE DEGREE OF

MASTER OF APPLIED SCIENCE

in

THE FACULTY OF GRADUATE STUDIES

Department Of Mechanical Engineering

We accept this thesis as conforming

to the required standard

THE UNIVERSITY OF BRITISH COLUMBIA

April 1983

In presenting this thesis in partial fulfilment of the requirements for an advanced degree at the University of British Columbia, I agree that the Library shall make it freely available for reference and study. I further agree that permission for extensive copying of this thesis for scholarly purposes may be granted by the Head of my Department or by his or her representatives. It is understood that copying or publication of this thesis for financial gain shall not be allowed without my written permission.

Department of Mechanical Engineering

The University of British Columbia
2075 Wesbrook Place
Vancouver, Canada
V6T 1W5

Date: April 25, 1983

Abstract

This thesis presents an experimental investigation on the drag of typical two-dimensional bluff bodies with a small circular cylinder (here called a "rod") placed upstream on the stagnation line. In most cases, the interaction was beneficial and the drag of the overall system was reduced. Fluctuating side force due to vortex shedding from the main body was also investigated for various rod positions and diameters.

Two typical bluff bodies were investigated: a circular cylinder and a flat plate. The front rod diameter (d) varied from 0.17D to 0.5D where D is the frontal width of the main circular cylinder or flat plate. Reynolds numbers defined using dimension D were in the range of 1×10^4 to 7×10^4, and the longitudinal spacing L from the rod centre to the main body was $0.4 < L/D < 7.0$.

For both the flat plate and the circular cylinder, the measured overall drag coefficient at various L/D showed a discontinuous "jump" at some critical spacing. This change corresponds to the elimination of the usual single stagnation point on the bluff body centre line and the appearance of two stagnation points symmetrically placed, close to the lateral edges of the body.

For the flat plate, the optimum configuration was found to be $d/D = 0.33$ at a spacing L/D of 1.81, and the overall drag reduction (based on the drag of the plate alone) was 36%. The drag reduction was due to a change in front

pressure only, the base pressure remaining essentially constant and independent of L/D. No Reynolds number dependence was found, as expected.

For the circular cylinder, the best overall drag reduction was found to be 58% for the configuration d/D = 0.33 and L/D = 1.73. Part of the drag reduction on the cylinder was due to the rod wake being turbulent which made the flow over the main cylinder critical, with a lower value of base pressure coefficient. The second effect was a sudden change in the front pressure distribution similar to that observed on the flat plate. Unlike the flat plate, however, the flow over the circular cylinder was sensitive to Reynolds number, with decreasing CD for increasing Re.

The fluctuating side force (Cl') on the cylinder due to vortex shedding was also investigated. The variation of Cl' with spacing followed different trends depending on the rod size and Reynolds number but Cl' never increased significantly with the use of the front rod and was reduced in most cases. The rod d/D = 0.17 seemed to be more suitable for minimum fluctuating side force. The position for Cl' minimum was found to depend upon the particular configuration.

Table of Contents

List of Tables

List of Figures

Nomenclature

CD	drag coefficient = (drag)/($0.5\rho U_1^2 HD$)
Cl'	fluctuating side force coefficient = (rms of side force fluctuation)/($0.5\rho U_1^2 HD$)
Cp	pressure coefficient = $(p-p_1)/(0.5\rho U_1^2)$
Cpb	base pressure coefficient
D	frontal width of the main body
d	rod diameter
F(z)	complex potential in the z-plane
f	frequency of vortex shedding (Hz)
H	test section height
h	plate width (potential flow model)
L	longitudinal spacing from the rod center to the main body
l_0	characteristic wake half-width
p	pressure on model surface
p_1	static pressure
Q	strength of sources
R	circle radius in ζ-plane
Re	Reynolds number
S	Strouhal number
U	free stream velocity in the z-plane
U_0	characteristic wake velocity deficit
U_1	free stream velocity
V	free stream velocity in the ζ-plane
w(z)	complex velocity in the z-plane
x	distance defining position on the surface of the flat plate

z	complex variable defining the flat plate plane
δ	angular position of source
Γ	circulation strength
ρ	density of air
ϕ	angle defining position on the surface of the circular cylinder
ψ	stream function
ζ	complex variable defining the circle plane
ζ_o	position of upper vortex in the ζ-plane
$\bar{\zeta}_o$	position of lower vortex in the ζ-plane

Acknowledgement

The author wishes to express his sincere gratitude to Professor I.S. Gartshore for his encouragement and valuable direction throughout this study.

Thanks are also due to the Department of Mechanical Engineering for the use of their facilities, and to the technical staff members for their valuable help during the construction of the wind tunnel models and during the experiments.

Special thanks to my fellow graduate students for their helpful advices and to my wife, Chantal, for playing the role of a student's wife so well.

Support for this research from the National Research Council of Canada is gratefully acknowledged. Computing facilities were provided by the University Computing Center.

I. INTRODUCTION

The purpose of this work is to investigate a new method of reducing mean drag and unsteady side force on a cylinder in a uniform flow.

1.1 Methods Of Reducing Fluid Forces

Different methods have been developed to reduce both drag and vortex shedding side force on a bluff body. Reducing these fluid dynamic forces is of great importance since it means possibly reducing the required strength of a structure, its weight and therefore its cost.

For a bluff body, the drag is a steady force in the direction of the flow largely due to boundary layer separation. The separated region, on the back of the body, is a region of low pressure whereas the front of the body is subjected to a higher pressure. This difference creates a steady force and the structure has to be designed to withstand this loading. Although there are unsteady components to the drag, these are usually small compared to the time averaged value and are not considered here.

The fluctuating side force is due to alternate shedding of vortices from each side of the cylinder. Each time a vortex is shed from the cylinder, the local pressure distribution is altered, creating a time-varying force on the cylinder, at the frequency of vortex shedding.

If the cylinder is rigid, the fluid dynamic forces are mainly a function of the shape of the body. But if the

cylinder deflects, an interaction of the displacement with the fluid forces may result which in turn can cause structural vibrations. The important parameters in this case are the shape of the body, the natural frequency and the damping of the structure.

In many cases, the fluctuating force due to vortex shedding is more important in the design of a structure than the drag. Important problems are associated with this fluctuating force such as material fatigue and synchronisation of vortex shedding frequency with the natural frequency of the structure.

There are basically two methods of reducing the fluid dynamic forces and vibrations on a cylinder:

(1) - Altering the shape of the body to reduce the amplitude and change the frequency of the force applied to the body.

(2) - Altering the natural frequency or damping of the structure to reduce the amplitude and change the frequency of oscillation.

A good review of available methods was made by Every et al.(1).

The first class of methods includes helical strakes, fairings, splitter plates, flags, perforated shrouds and others. These methods are based on an alteration of the shape of the structure in order to change the boundary layer separation points, prevent or reduce the formation of vortices and prevent the correlation of vortex shedding

along the length of the structure.

Some of these devices reduce vortex shedding but increase drag (helical strakes); some reduce both but are expensive (fairings) or not very efficient (splitter plates); some are unidirectional (fairings), others are omnidirectional (helical strakes).

The second class of methods includes the use of dampers, stiffeners and different materials in order to change the natural frequency and damping of the structure.

1.2 Bluff Body Interaction

It is known that two bluff bodies placed in line in a uniform stream can lead, in some cases, to a total drag significantly lower than that of either body alone. Morel & Bohn (2) investigated the flow over two disks of unequal diameter placed in tandem and Roshko & Koenig (3) investigated the flow over a flat faced circular cylinder preceded by a concentric circular disk. They both found a remarkable drag reduction from the value of the reference body. Morel & Bohn showed a drag reduction of 81% in the optimum case.

This idea is used in this work to design a device that could be used on two-dimensional structures to reduce drag and vortex shedding side force. Through wind tunnel experiments, the flow over typical bluff bodies with a small circular cylinder placed upsteam on the stagnation line is investigated. Two typical bluff bodies are studied: a flat plate and a circular cylinder.

Igarashi (4) has already investigated the characteristics of the flow over two circular cylinders with ratio d1/d2 = 0.68, the smaller cylinder being downstream. The existence of different flow patterns varying with spacing and Reynolds number was shown.

Zdravkovich & Pridden (5) investigated the interaction between two circular cylinders of the same size placed in tandem. Hiwada et al.(6) looked at the fluid flow and heat transfer around two circular cylinders of different diameters in tandem. The smaller cylinder was placed upstream and used as a turbulence generator.

1.3 Objective

In all previous works on the interaction of two-dimensional bluff bodies, different flow patterns were identified at different spacing ratios. However, no work has yet been done to identify the optimum spacing for least overall drag or for least vortex shedding side force. This is the objective of this work.

In the following experiments, the front circular cylinder, from now on called the front rod, is relatively small compared to the main body. Its diameter is varied from 0.17 D to 0.50 D, where D is the frontal width of the main body. Since the front rod is used as a method for drag or vortex shedding reduction on a bluff body, its size must be kept small to make it cost competitive with other methods of force reduction.

Experiments are carried out, firstly using a flat plate as the main body and secondly using a circular cylinder. The results for the flat plate should be independent of Reynolds number and there is no significant side force present. The parameters varied are the spacing L, the rod diameter d and the Reynolds number Re. The flat plate coordinate system and symbols are defined in Fig.1(a).

The experiments using a circular cylinder as the main body are carried out varying the same parameters, but this time the fluctuating side force is measured and the Reynolds number is expected to be an important parameter. The circular cylinder coordinate system and symbols are defined in Fig.1(b).

II. DESCRIPTION OF APPARATUS AND EXPERIMENTS

2.1 Smoke Tunnel

A smoke tunnel (Fig.2) was used for flow visualisation. It is an Elektron open circuit wind tunnel, with a two-dimensional test section. Its test section is 558 mm long with a cross section of 29 mm by 330 mm. The two-dimensional model was placed 150 mm downstream of the end of the contraction.

Smoke was injected ahead of the model by a series of 29 horizontal nozzles. The smoke, following the air flow, made the flow pattern visible. The smoke was generated by burning pipe tobacco and its flowrate could be adjusted.

The maximum Reynolds number based on the model cross section was 5×10^3. Pictures of different arrangements were taken.

2.2 Wind Tunnel

The quantitative experiments were conducted in the U.B.C. low speed, low turbulence, closed return type wind tunnel in which the velocity can be varied from 0 to 46 m/s with an inherent undisturbed turbulence level of less than 0.1%. The spatial variation of mean velocity in the test section is less than 0.25%.

Three screens smooth the flow at the entrance of the settling chamber and a 7:1 contraction accelerates the flow, improving its uniformity as it reaches the test section. The test section is 2.74 m long with a cross-section of

914 mm by 686 mm. Four fillets decreasing from 152 mm at the upstream to 121 mm at the downstream end offset the effect of boundary layer growth in the test section.

The tunnel is powered by a 15 HP direct current motor driving a commercial axial flow fan with Thyristor speed control.

The pressure differential across the contraction is measured on a Betz micromanometer which can be read to 0.02 mm of water. The test section velocity is calibrated against the above pressure difference. Fig.3 shows an outline of the tunnel.

2.3 Wind Tunnel Balance

Force measurements on models were taken on an Aerolab strain gauge balance. For the purpose of this experiment, only the mean drag was read from the balance. The frequency response of the balance is much too low to allow its use in the measurement of fluctuating side force.

2.4 Models

Each model consisted of two parts: the downstream main bluff body and the upstream rod. The two main bluff body models used (a flat plate and a circular cylinder) had same frontal width of 38.1 mm. Three different diameters of front rod were used: 6.35, 12.7 and 19.1 mm, giving non-dimensionalised rod sizes d/D of 0.17, 0.33 and 0.50.

The main body was fixed to a stand while the front rod was fixed to a support which was movable on the stand so

that the axis of the two cylinders would stay in the direction of the free stream. The models vertically spanned all the way across the wind tunnel and extended outside. The two parts were connected together on the balance so that the drag measured was the total force on the two parts (Fig.4).

End plates were mounted on each model at a distance of 38 mm from the wind tunnel roof and floor, so that they were just outside the tunnel wall boundary layers.

Stansby (7) showed that the end effects on a two-dimensional circular cylinder without end plates altered the true base pressure over the entire length of the model, even when the aspect ratio was as high as 20. It was shown that this change in base pressure could be rectified by the use of end plates.

Lee (8), doing related work on square sections, concluded that in the case of two-dimensional models with sharp corners, the utilisation of end plates was of little use.

In this work, both circular cylinder and sharp corner models were used. Since end plates seem to be compulsory for the circular cylinder, end plates were used for consistency on all models including the flat plate.

There was a second reason for using end plates; because a balance was used to measure the drag, a gap was left around the model where it passes through the wind tunnel roof and floor; from this gap, air could be sucked in or out

due to the pressure difference and the pressure distribution on the model could be affected. End plates were assumed to minimize this effect.

The end plates were designed according to Stansby's recommendations (Fig.5). The front rod end plates were of various sizes to suit different rod spacings and avoid interference.

2.5 Pressure Distribution Measurements

All models were fitted with pressure taps at their mid-span position. For the flat plate, seven pressure taps were distributed on the front and one pressure tap was located at the back. The pressure at the back was assumed constant across the width of the plate, an assumption that was verified experimentally. For the circular cylinder, pressure taps were located at 20° intervals all around, except near the base where the pressure is essentially constant (see Fig.29). One pressure tap was located at mid-span on the 12.7 mm diameter front rod, and pressure measurements at various angles were made by rotating the rod. For the other two rods, 6.35 and 19.1 mm diameter, the pressure distribution was not measured. Fig.6 shows the location of pressure taps on the models.

Pressure measurements were made using a Setra 237 differential pressure transducer in a scanivalve. The pressure transducer was calibrated against the wind tunnel Betz manometer and the calibration was frequently checked. The pressure taps were connected to the scanivalve through 1

m of tygon tubing with internal diameter of 1.68 mm. The reference pressure was the static pressure in the test section.

2.6 Mean Drag Measurements

The overall drag of the two parts of the model, front rod and main cylinder, was measured by the balance. A drag coefficient was calculated from the measured force, the frontal area of the main cylinder and the dynamic pressure of the flow. The frontal area was taken as the height of the test section multiplied by the dimension D of the model.

An error in the measured drag coefficient was introduced due to end effects and friction on the end plates. This error in drag was assumed to be proportional to the total drag on the model. A calibration was made between the balance reading (total force on the model) and the force measured by integration of the pressure distribution (force on the mid-span section of the model). Fig.7 shows the calibration curve, using different models, from which a calibration constant of 1.048 was deduced; all later balance drag coefficients were corrected in this way:

$$CD(\text{true}) = 1.048\ CD(\text{balance})$$

2.7 Fluctuating Side Force Measurements

Side force measurements were only taken on the circular cylinder. A different arrangement of pressure taps was used; eight pressure taps were located on one side of the cylinder in such a way that their average pressure was proportional to the side force. Details of the calculations of the pressure tap location are shown in Appendix A.

The averaging of the pressure was made using the technique for pneumatic averaging as described by Stathopoulos (9). The eight pressure tubes were connected to a special symmetrical manifold designed to have minimum possible internal volume. The manifold had a single output tube which was expected to give a measurement of the average of the eight input pressures. Stathopoulos showed that this system works well and has a good frequency response, at least at low frequencies (below about 60 Hz depending on tubing connections used). Fig.8 shows a sketch of the manifold.

Because the tubing system, the manifold and the transducer cavity introduce frequency dependent distortion of the pressure fluctuations, the side force measuring system was calibrated. A schematic representation of the calibration apparatus is shown in Fig.9. A fluctuating pressure was created in the cylinder by a fluctuating diaphragm. The diaphragm was activated by a vibrator connected to a frequency generator. Nine pressure taps were fitted to the cylinder head so that one could be used as a

reference while the other eight were connected to the manifold.

The reference pressure was measured by the scanivalve through a short length of tubing (50 mm). The output pressure of the system to be calibrated was also measured by the scanivalve on a second channel. The amplitude ratios ($RMS/RMS_{ref.}$) were plotted against frequency for frequencies between 8 Hz and 240 Hz. The result, called the transfer function, is shown in Fig.10.

Four cases are shown where eight, six, four and two manifold inputs were connected to the cylinder head, the other inputs being left open to ambient pressure. The reference value was taken as the average fluctuation of the eight manifold inputs, if no distortion due to frequency existed. In the case of four inputs left open, for example, the reference value was half of the amplitude read at the cylinder reference tap. There is good agreement between the four different configurations even at high frequencies, which shows that the averaging method works well even at frequencies as high as 240 Hz. The only inconsistency in the results is around the resonant peak (~60 Hz) and could be a source of error.

The solid curve in Fig.10 is used in Chapter IV to correct fluctuating side force readings for frequency distortion.

A Spectrascope II frequency analyser was used during the experiment to measure the frequency spectrum and as a

result the dominant frequency of vortex shedding.

2.8 Data Acquisition

Signals from both the balance and the pressure transducer were digitized by a NEFF Data Acquisition System. Digital signals were then processed by a PDP-11/34 computer. The sampling rate was set to 400 Hz and sampling time was 10 seconds. From these 4000 readings, the average and the RMS value of the fluctuation were calculated.

The program would also transform these values into coefficient form as follows:

$$Cp = (p - p_1)/(0.5\rho U_1^2)$$

$$CD = (Drag)/(0.5\rho U_1^2 DH)$$

where $p - p_1$ is given by the pressure transducer

$0.5\rho U_1^2$ is given by the Betz manometer

Drag is given by the balance

DH is given by 38.1 mm x 685.8 mm (model frontal width multiplied by wind tunnel height)

III. RESULTS AND DISCUSSION I: FLAT PLATE

Tests were conducted on the flat plate with two sizes of front rod, d/D = 0.17 and d/D = 0.33, at three Reynolds numbers (2.5×10^4, 4×10^4 and 5×10^4) based on D. No Reynolds number dependence was found, as expected. Similar tests were conducted in the smoke tunnel for visualisation purposes at a Reynolds number of 5×10^3.

3.1 Pressure Distribution On Flat Plate

In the wind tunnel, the plate was aligned perpendicular to the air stream by rotating the model until the pressure distribution on the front face was symmetrical.

The mean pressure distribution on the flat plate is shown in Fig.11. These results, as well as all later values of Cp and CD, have been corrected for wind tunnel blockage using Maskell's method (10) with the blockage being 4.1%. This pressure distribution is compared with Fage & Johansen's results (11), corrected for blockage, and Parkinson's wake source model (12). Numerical integration of the pressure distribution gives a value of drag coefficient CD = 1.94 as compared with the calibrated balance reading CD = 1.95 and with Fage & Johansen's value of CD = 1.90. There is a discrepancy between Fage & Johansen's results and the current results, mainly in the base pressure value. This is probably due to a difference in thickness to width ratio. The model used in this experiment had a thickness to width ratio of 1/12 while Fage

& Johansen's model had sharp edges. Engineering Science Data (13) shows that the effect of a thickness to width ratio of 1/12 is about the same as observed here.

3.2 Pressure Distribution On Flat Plate With Front Rod

The mean pressure distribution on the flat plate when the front rod d/D = 0.33 was located between L/D = 7.17 and L/D = 1.97 is shown in Fig.12. Fig.13 shows the pressure distribution on the same model, when the rod was located between L/D = 1.81 and L/D = 0.84.

Two different flow regimes are observed. The first, regime A, is observed for $\infty > L/D > 1.97$ and the second, regime B, for $1.97 > L/D > 0.84$. The flow at spacing L/D = 1.97 was found to be bistable, switching from one regime to the other. No experiments were done with L/D less than 0.84.

Similar results were obtained when the rod d/D = 0.17 was used. Pressure distributions are shown in Fig.14 for regime A and in Fig.15 for regime B.

The pressure distribution on the front rod d/D = 0.33 at two different spacings has been measured and the results are shown in Fig.16. The pressure distribution at spacing L/D = 3.42 (flow regime A) is very similar to a subcritical pressure distribution around a circular cylinder in a uniform flow. At spacing L/D = 1.42 (flow regime B) the strong interaction of the two bodies makes the rod base pressure have a constant and higher value than the previous case.

3.3 Flow Regime A

The characteristics of this flow regime (Figs.12 & 14) are that the pressure on the front of the plate decreases with decreasing rod spacing and that the base pressure remains constant, independent of the rod position.

The decreasing front pressure with decreasing spacing can be explained by the fact that it is not a uniform flow that reaches the plate, but a flow with the typical mean velocity profile of a wake behind a circular cylinder.

The plane wake behind a circular cylinder in a uniform stream has been carefully studied by Townsend (14). The mean velocity profile in the wake is characterised by a velocity deficit at the center, U_0, decreasing with increasing downstream distance and by a characteristic wake width, l_0, increasing with downstream distance. For a small deficit wake, similarity arguments showed that $U_0 \propto x^{-1/2}$ and $l_0 \propto x^{1/2}$, when x is measured in the streamwise direction from an appropriate origin.

If the plate does not have a strong interaction with the rod wake, the stagnation pressure at the centre of the plate can be considered as a measure of the total head at the centre of the wake. The static pressure can be assumed to be constant across the flow and the velocity deficit of the wake can be found from the measured stagnation pressure at the centre of the plate, p(centre):

$$Cp(centre) = (p(centre) - p_1)/(0.5\rho U_1^2)$$

$$= (0.5\rho U(centre)^2)/(0.5\rho U_1^2)$$

$$= (U(centre)/U_1)^2$$

$$U_0 = U_1 - U(centre) = (1 - \sqrt{Cp(centre)})U_1$$

The values of velocity deficit on the centre line, as calculated $(1 - \sqrt{Cp(centre)})U_1$, are tabulated for both sizes of rod in Table I, and should be proportional to $x^{-1/2}$.

Fig.17 shows U_0/U_1 versus L/d, distance non-dimensonalised with respect to the rod size. The curve $U_0/U_1 = (L/d)^{-1/2}$ is also shown and follows the data points well. This result is in good agreement with Townsend who showed that on the centre line of a wake behind a circular cylinder:

$$(U_0/U_1)(L/d)^{1/2} \cong 1$$

This last figure well supports the explanation that the front stagnation pressure coefficient is less than one due to the velocity deficit of the wake of the rod.

The second characteristic of regime A, which is also a characteristic of regime B, is a base pressure essentially independent of rod position. Fig.18 shows the base pressure coefficient versus spacing for the two sizes of rod. There is some scatter but the base pressure coefficient is fairly

constant around -1.24. Turbulence in the flow does not seem to be an important factor governing the base pressure value, probably because of the fixed separation points and no possibility of reattachment.

The wake velocity profile does not seem to affect the base pressure either. If the velocity profile in the wake of the front rod is consistent with Townsend's results as it seems to be from Fig.17, then the characteristic wake width, l_o, which would exist in the absence of the plate, can be evaluated. Townsend showed that:

$$l_o \cong 0.4(Ld)^{1/2} \quad \text{(half width to half depth)}$$

From the last equation, values of l_o/D were calculated and are shown in Table I. l_o/D is always smaller than 0.5 or l_o always smaller than the plate half-width, except when the rod is far and has a weak effect. Therefore, the velocity at the edge of the plate is expected to keep a constant value so that the base pressure is also constant.

3.4 Flow Regime B

This flow regime is completely different from the typical flow over a flat plate alone. The two bodies have a strong influence on each other, substantially affecting the flow field. This change in flow pattern begins at one typical spacing, that we will call the critical spacing.

Flow visualisation pictures (Fig.19) show a change in flow pattern occurring between L/D = 1.36 and L/D = 0.79.

The pattern in Fig.19(a) shows a typical wake behind a circular cylinder in the region between the rod and the plate for L/D = 1.36. A different flow pattern is shown in Fig.19(b) for L/D = 0.79. A closed region between the plate and the rod is formed where recirculation occurs. The two separated shear layers from the rod reach the plate very close to the edges of the plate.

Because of the strong blockage and the two-dimensional test section of the smoke tunnel, the visualisation results show a lower value of critical spacing than that shown in the wind tunnel. Nevertheless, the flow visualisations are helpful in understanding the different regimes.

In regime B (Figs.13 & 15), instead of one stagnation point at the centre, the pressure distributions show two symmetrical near-stagnation points close to the edges of the plate. They represent the reattachment of the separated shear layers of the rod onto the plate. Their value is less than Cp = 1 because of losses in the shear layers and unsteadiness.

The exact location and pressure of these near-stagnation points could not be measured because they were located between the edge of the plate and the first pressure tap. But from the pressure distributions in regime B, there must be a point of maximum pressure between the edge of the plate (pressure given by the base pressure measurement) and the first pressure tap.

The pressure distribution on the central portion of the

plate, say $0.3 < x/D < 0.7$, is fairly constant. For the rod $d/D = 0.33$ at spacing $L/D = 1.42$, this constant value is approximately $Cp = -0.10$ and is the same as the front rod base pressure at the same spacing (Fig.16). This supports the idea that a closed region is formed between the rod and the plate, where the mean velocity is small and where the pressure is essentially constant.

The change in pressure distribution with spacing for regime B, is an increasing front pressure with decreasing spacing. The fact that the closed region gets smaller with smaller spacing suggests that less dissipation due to turbulence occurs at smaller spacing and hence an increase in front pressure.

As already pointed out, the plate base pressure is fairly constant whatever the position of the rod (Fig.18).

3.5 Drag

Fig.20 and 21 show drag coefficient versus rod spacing for the two rods, $d/D = 0.33$ and $d/D = 0.17$ respectively. Each graph shows the overall drag coefficient measured by the balance and the drag coefficient of the plate only, calculated by numerical integration of the pressure distribution. The drag coefficient of the rod is given by the difference between the two curves.

A minimum drag coefficient is reached at the critical spacing. For the rod $d/D = 0.33$ the minimum CD is 1.25 occurring at $L/D = 1.81$, as compared to 1.94 for the plate alone; this is a drag reduction of 36%. For the rod

d/D = 0.17 a maximum drag reduction of 24% is achieved at the critical spacing, L/D = 1.64.

The change in flow pattern is represented by a dotted line because the drag coefficient drastically drops when the flow pattern switches from regime A to regime B. At this point the flow was found to be bistable.

The drag of the rod keeps a fairly constant value in each regime and is always smaller than the drag of the same rod in a uniform flow.

The overall drag coefficient decreases with decreasing spacing in regime A and increases with decreasing spacing in regime B.

3.6 Effect Of Yaw

Since the drag reduction device investigated is unidirectional and, in practical cases, the structure may not be perfectly aligned with the flow, it is of interest to study the effect of small yaw angle on the drag.

The overall drag coefficient versus yaw is shown in Fig.22 when the rod d/D = 0.33 was located at spacing L/D = 1.42 (regime B). The measured drag coefficient is divided by $CD_{ref.}$ which is the drag coefficient of the plate alone at zero yaw. The drag reduction is 34% at 0° and is only 17% at 12°. The effect of yaw is therefore important and the device should be aligned with the flow as much as possible if a large drag reduction is to be achieved.

3.7 Effect Of Reynolds Number

As expected, Reynolds number did not have much effect on pressure coefficient because the separation points are fixed at the edges of the plate.

The results at the three differents Reynolds numbers, 2.5×10^4, 4×10^4 and 5×10^4, were exactly the same within the accuracy of measurements.

3.8 Potential Flow Model

A two-dimensional incompressible potential flow model is presented here and was developed as a numerical experiment. It represents the flow over the flat plate in regime B. The blockage due to the rod was assumed to be of little importance, the main effect of the rod being to fix the upstream stagnation point and create a wake independant of rod shape or size.

In this model, the normal flat plate is mapped from a circle by the Joukowski transformation. The representation of the separated flow behind the plate is obtained using Parkinson's wake source model (12). The separated flow created by the rod upstream the flat plate is represented by a symmetrical pair of vortices.

Consider the wake source model for a normal flat plate as shown in Fig.23. The complex potential of the resulting flow in the ζ-plane is:

$$F(\zeta) = V\left(\zeta+\frac{R^2}{\zeta}\right)+\frac{Q}{\pi}\{\ln(\zeta-Re^{i\delta})+\ln(\zeta-Re^{-i\delta})-\ln\zeta\}$$

and the complex velocity is:

$$w(\zeta) = V\left(1-\frac{R^2}{\zeta^2}\right)+\frac{Q}{\pi}\left(\frac{1}{\zeta-Re^{i\delta}} + \frac{1}{\zeta-Re^{-i\delta}} - \frac{1}{\zeta}\right)$$

The Joukowski transformation, which preserves velocity at infinity, transforms the circle into a normal flat plate:

$$z = \zeta - R^2/\zeta \qquad \text{where } R = h/4$$

The boundary conditions are:

(1) stagnation points in the ζ-plane at the critical points of the transformation so that the angles are doubled there and the flow leaves the plate tangentially:

$$w(\zeta) = 0 \qquad \text{at } \zeta = \pm iR$$

(2) the base pressure is specified. At the critical points, $w(z)$ is finite and :

$$w(z) = U(1 - Cpb)^{1/2} \qquad \text{at } z = \pm h/2$$

From these two conditions, Q and δ are determined.

Now to add a symmetrical pair of vortices in front of the circle (at ζ_0 and $\bar{\zeta}_0$) in order to create a bubble, we also have to add images inside the circle to satisfy the circle boundary conditions. The location (ζ_0) and strength (Γ) of the pair of vortices will determine the size of the bubble. The complex potential becomes:

$$F(\zeta) = V\left(\zeta+\frac{R^2}{\zeta}\right)+\frac{Q}{\pi}\{\ln(\zeta-Re^{i\delta})+\ln(\zeta-Re^{-i\delta})-\ln\zeta\}+$$
$$\frac{i\Gamma}{2\pi}\{\ln(\zeta-\zeta_o)+\ln(\zeta-R^2/\zeta_o)-\ln(\zeta-\bar{\zeta}_o)-\ln(\zeta-R^2/\bar{\zeta}_o)\}$$

and the velocity potential:

$$w(\zeta) = V\left(1-\frac{R^2}{\zeta^2}\right)+\frac{Q}{\pi}\left(\frac{1}{\zeta-Re^{i\delta}}+\frac{1}{\zeta-Re^{-i\delta}}-\frac{1}{\zeta}\right)$$
$$+\frac{i\Gamma}{2\pi}\left(\frac{1}{\zeta-\zeta_o}-\frac{1}{\zeta-\bar{\zeta}_o}+\frac{1}{\zeta-R^2/\zeta_o}-\frac{1}{\zeta-R^2/\bar{\zeta}_o}\right)$$

with again the Joukowski transformation and the conditions:

(1) $w(\zeta) = 0$ at $\zeta = \pm iR$

(2) $w(z) = U(1 - Cpb)^{1/2}$ at $z = h/2$

and extra conditions to determine the location and strength of vortices. A condition determining both the location and the strength of the vortices at the same time was used here. The condition is that each vortex be stationary, which means that the velocity at its location due to all singularities except itself, is zero:

$$w'(\zeta) = V\left(1-\frac{R^2}{\zeta^2}\right)+\frac{Q}{\pi}\left(\frac{1}{\zeta-Re^{i\delta}}+\frac{1}{\zeta-Re^{-i\delta}}-\frac{1}{\zeta}\right)$$
$$+\frac{i\Gamma}{2\pi}\left(\frac{1}{\zeta-R^2/\zeta_o}-\frac{1}{\zeta-R^2/\bar{\zeta}_o}-\frac{1}{\zeta-\bar{\zeta}_o}\right) = 0 \qquad \text{at } \zeta = \zeta_o$$

From these conditions, we can determine a locus of vortex positions where Q, Γ and δ can also be determined. Fig.24 shows the streamlines of the flow over the flat plate with the front stagnation point at L/D = 0.87. The base pressure was specified as Cpb = -1.24 as found experimentally in a previous section.

It is noticed that the size of the bubble seems to be too large and, as a result, the streamlines go over the plate quite smoothly, creating a much narrower wake than expected. Even though the streamlines look very smooth when passing over the plate, the streamline $\psi = 0$ leaves the plate tangentially and curves downstream very rapidly.

This is a rather poor simulation of the streamlines if we compare this with the flow visualisation picture of Fig.19(b). This result could be improved by choosing a vortex strength and position that would satisfy the first two boundary conditions and also give a good streamline representation.

One might be interested in evaluating the drag from the present model. The real flow is obviously not potential inside the bubble and the pressure must be prescribed empirically. From the experiment, the pressure inside the bubble is fairly constant, it would therefore make sense to use a constant value of pressure.

If the pressure is specified inside the bubble, and since the base pressure is also specified, only the pressure near the edges of the plate can be varied by the model, which would not change the total drag significantly.

In conclusion, the model is not useful to predict the drag and, in its present form, does not give realistic streamlines shape. A better condition for Γ and ζ_0 could improve the model as far as streamlines are concerned. But this "better" configuration would have to be found by trial

and error.

This model shows the limitations of potential flow in representing separated flow but it may be useful in representing how much a change in parameters, such as the base pressure, can affect the outer flow.

IV. RESULTS AND DISCUSSION II: CIRCULAR CYLINDER

The flat plate was replaced by a circular cylinder of the same frontal width, 38.1 mm, and the same types of measurements were carried out. In this case, unlike the flat plate, the Reynolds number was expected to be an important parameter governing the flow. The fluctuating side force, significant in this case, was also measured. Experiments were carried out in the wind tunnel for Reynolds numbers in the range 1.0×10^4 to 7.0×10^4. Similar experiments were done in the smoke tunnel at a Reynolds number of 5×10^3.

4.1 Pressure Distribution On Circular Cylinder

4.1.1 Background

In the range of Reynolds number of interest for aerodynamicists, between 10^3 and 10^7, the flow over a circular cylinder is subjected to different flow patterns. Fig.25 shows the drag coefficient, CD, in this range of Re, taken from Achenbach (15). Four ranges are specified: subcritical, critical, supercritical and transcritical.

In the subcritical range, the flow is not influenced by the surface roughness and the drag coefficient is essentially constant. At higher Re, CD suddenly drops. This is due to the laminar boundary layer separation and the turbulent reattachment. Turbulent mixing re-energizes the decelerating boundary layer, making the final separation occur further downstream. It results in a narrower wake

(low pressure region) corresponding to a fall in drag coefficient. Exceeding the Reynolds number of CD minimum, the drag coefficient increases again in the supercritical range and reaches a nearly constant value in the transcritical range.

Near the critical Re, at which CD drops sharply, it is known that the flow pattern is strongly dependent on the turbulence level of the approaching stream and on the roughness of the surface. Achenbach showed that the effect of turbulence was mainly to shift the curve CD versus Re to the left so that the flow becomes critical at a lower Re.

4.1.2 Results

Measured pressure distributions around the circular cylinder alone at different Reynolds numbers in the subcritical range are shown in Fig.26. The solid line represents the pressure distribution around a circular cylinder in the subcritical range, as shown in Engineering Science Data (16). The data points do not follow exactly the solid line, first, because they have not been corrected for blockage and second, because they represent pressure distributions at various Reynolds numbers. Despite some discrepancies, the data points are in good agreement with the solid line.

The uncorrected value of drag coefficient for $3.3 \times 10^4 < Re < 7.1 \times 10^4$, as measured by the balance, was found to be constant with CD = 1.19. This value will be used later as the reference value.

As mentioned above, the data points have not been corrected for blockage as is the case for all the results in this chapter. It has been shown recently by West & Apelt (17) that when two well known methods for blockage correction, one of them being Maskell's (10), are applied to a circular cylinder the corrected values of drag coefficient are not any closer to the values free of blockage effects. On the other hand, the corrected value for base pressure using Maskell's method is very close to the expected value. The suggested explanation was that the shape of the pressure distribution, such as the location of the separation points, is changed by the blockage. As a result the correction, which is made only by resizing the pressure distribution curve without changing its shape, introduces an error. Therefore the values of drag and pressure coefficient in this chapter were not corrected for blockage even though it has been a common practice in previous works.

One value of base pressure is corrected here by Maskell's method in order to compare it with other quoted values. For the circular cylinder at $Re = 6.5 \times 10^4$, the corrected base pressure coefficient is -1.30 as compared with ESDU's value (16) of -1.23 for this range of Reynolds numbers.

4.2 Pressure Distribution On Circular Cylinder With Front Rod

The pressure distribution on the cylinder was measured when a rod was located upstream at various spacings. Three sizes of front rod were used, $d/D = 0.17$, $d/D = 0.33$ and $d/D = 0.50$. The experiments were done at three different Reynolds numbers, 1.0×10^4, 3.3×10^4 and 6.5×10^4. The nine resulting graphs are presented in Figs.27 to 35.

For clarity, each graph is presented in two parts, (a) and (b). The two flow regimes, A and B described in the previous chapter, still occurred for the circular cylinder. For each graph, (a) represents regime A while (b) represents regime B.

The nine graphs have the same general characteristics which will be discussed in the following sections. In most cases, the changes in pressure distribution are progressive with rod spacing except for the low Reynolds number, 1.0×10^4, where the inaccuracy of the pressure measurements makes the results show some scatter.

4.3 Flow Regime A

The effect of the front rod on the cylinder front pressure distribution is similar to that described for the flat plate. The front stagnation pressure coefficient is less than one and is decreasing with decreasing rod spacings. This is due to the velocity deficit of the front rod wake and it would be possible to present a similar graph of U_0/U_1 versus L/d as for the flat plate.

Unlike the flat plate, the circular cylinder base pressure is affected by the position of the rod. The rod creates turbulence in the stream reaching the cylinder. As mentioned in section 4.1, turbulence makes the separation points occur further downstream on the surface of the cylinder, permitting a more complete pressure recovery. The proximity of the rod increases the turbulence level and therefore the base pressure.

For example, at $Re = 3.3 \times 10^4$ when the rod is absent (Fig.26), the base pressure, 180° from the front stagnation point, is $Cpb = -1.32$. By bringing the rod $d/D = 0.17$ closer to the cylinder, the base pressure increases (Fig.28(a)). At a certain spacing, the base pressure becomes almost constant with decreasing spacing and remains constant at $Cpb = -0.83$ until the change in flow regime. The separation points are therefore expected to have been shifted downstream by bringing the rod closer.

The solid line in Fig.28(a) represents the pressure distribution for critical flow around a circular cylinder, taken from Engineering Science Data (16). Good agreement is found between the shape of the solid curve and the present data at small spacings ($L/D < 2.4$), except for the front stagnation point. This suggests that the effect of turbulence is to make the flow critical.

The trends of the group of curves are, in regime A, toward a larger base pressure value for larger rod diameters and larger Reynolds numbers.

4.4 Flow Regime B

A different flow regime occurs because of the strong interaction between the rod and the cylinder at smaller spacings. Again, like the flat plate, two symmetrical stagnation points are formed as well as a closed region of roughly constant pressure. The main difference with the flat plate results is that the base pressure is influenced by the rod position. It seems that the separation occurs earlier when the rod gets closer in regime B because the base pressure decreases with decreasing spacing.

The trends of this group of curves are similar to those of regime A, toward a larger base pressure for larger rod diameters and larger Reynolds numbers.

4.5 Drag

Only the total drag of the two parts of the model was looked at in the case of the circular cylinder, since it was known from the flat plate results (section 3.5) that the drag of the rod itself was not important. Its value was almost constant in each flow regime and always smaller than the drag of the same rod in a uniform flow. Therefore, only the balance measurements were plotted.

Fig.36 shows the overall drag at $Re = 3.3 \times 10^4$ and 6.5×10^4 for the front rod $d/D = 0.17$. Figs.37 and 38 shows similar results for $d/D = 0.33$ and $d/D = 0.50$ respectively. The third Reynolds number, 1.0×10^4, is not represented here because balance readings were very inaccurate as the force was very small.

The shape of each plot is similar to the flat plate results. In regime A, the overall drag decreases with decreasing spacing. Then there is a sudden jump in the curve at the critical spacing corresponding to a change in flow pattern. The minimum drag is obtained at that critical spacing. Then, if the rod is brought closer in regime B, the drag increases again.

The main difference between the flat plate and the circular cylinder results is that there is already an important drag reduction for the circular cylinder when the rod is quite distant, say L/D = 7, whereas there was no significant drag reduction at that spacing for the flat plate. The drag reduction on the cylinder in regime A is due to the turbulence created by the rod; this makes the flow enter the critical region, decreasing its drag.

An extra reduction is obtained at the critical spacing when the flow switches to regime B. This extra drag reduction is due to a change in front pressure only, the base pressure being essentially the same as that just before the critical spacing.

For example, in the case of d/D = 0.33 at Re = 6.5×10^4 (Fig.37), the drag reduction just before the critical spacing (regime A) is already 34% (CD = 0.78) and at the critical spacing it is 58% (CD = 0.50). The difference, 24%, is mainly due to a change in the cylinder front pressure.

4.6 Effect Of Reynolds Number

In the range of Reynolds numbers studied, the main effect of increasing Re was to lower the overall drag, shifting the curve of drag versus spacing downwards (Figs.36 to 38). This result can be explained by the fact that the Reynolds number around the cylinder is increased, bringing the flow closer to the critical range, improving the base pressure recovery and reducing the drag coefficient. Another possible explanation is an increase in turbulence reaching the cylinder due to a higher Reynolds number around the front rod.

4.7 Optimum Configuration

It has been shown that at any Reynolds number there is a rod position giving a minimum drag, this position corresponding to the critical spacing. The important parameters governing the optimum configuration are:

(1) - size of rod d/D

(2) - spacing L/D

(3) - Reynolds number Re

Fig.39 shows the effect of rod size on the minimum drag for two Reynolds numbers. At $Re = 6.5 \times 10^4$, a drag reduction of 58% is achieved with a relatively small rod, $d/D = 0.33$. At lower Reynolds numbers, the drag reduction is less and the size of the rod must be larger for maximum drag reduction. A drag reduction of 44% is achieved at $Re = 3.3 \times 10^4$ with the rod $d/D = 0.50$ but a lower drag could probably be achieved with an even larger rod.

Fig.40 shows the critical spacing for different rod sizes and Reynolds numbers. The critical spacing is always in the range $1.2 < L/D < 2.4$. It was assumed that the position of the critical spacing was between the last value in regime A and the first value in regime B. The results show some scatter but the trend is toward a larger critical spacing for larger rod diameters and for larger Reynolds numbers.

The Reynolds number had a strong effect on the minimum drag (Fig.37 to 39). Unfortunately, for many practical applications the Reynolds number will be higher than the maximum value investigated here (the maximum value of the experiment, 6.5×10^4, was fixed by limits of the instrumentation). For higher Reynolds numbers it is expected that the minimum drag coefficient will be even lower. On the other hand, the reference drag coefficient (cylinder in uniform flow) will be lower because the flow may be in the critical range. Therefore the drag reduction could be consequently lower than for the range of Reynolds numbers studied here. No change in trend is anticipated at high Reynolds number however.

4.8 Effect Of Yaw

The effect of small yaw on the drag was looked at but the results were very inaccurate because the model was not designed for that purpose. From the results gathered, the trend of the drag with yaw seems to be similar to that of

the flat plate.

4.9 Fluctuating Side Force

The fluctuating side force due to vortex shedding on a circular cylinder alone has its frequency and intensity changing with Reynolds number. However in the range of Reynolds numbers investigated the non-dimensional frequency, the Strouhal number $S=(fD)/U_1$, is constant. This was verified experimentally and the results are presented in Fig.41(a), giving S = 0.195. This result well agrees with the value of S = 0.20 generally accepted.

The intensity Cl', given by the RMS value of the fluctuating force, was measured by the method described in Chapter II. The results (Fig 41(b)) are shown in two sets of data points: one is corrected for frequency distortion by the transfer function (Fig.10), the second is left uncorrected. Other curves by Keefe (18) and Gerrard (19) are also shown. None of the results seem to agree, probably because of different turbulence levels. It has been shown by Gerrard (20) that in this range of Reynolds numbers the oscillating side force is remarkably sensitive to turbulence level.

4.10 Side Force On Model With Front Rod

The fluctuating side force was investigated to make sure that no problem was created by the front rod. Fig.42 shows the fluctuating side force on the cylinder with the rod d/D = 0.17 at different spacings. Similar results for

d/D = 0.33 and d/D = 0.50 are shown in Figs.43 and 44 respectively. The measured values of Cl' were not as accurate as the other results because of the method of measurement. Therefore these values should not be considered as definitive.

For the small rod (d/D = 0.17) the result at Re = 1.0×10^4 shows considerable scatter and is difficult to interpret. The reason is probably a sampling time too small (10 sec.) for the low frequency involved(~20 Hz). This result is therefore discarded as well as results at the same Re for the other rod diameters.

The behaviors of the six remaining curves (Figs.42 to 44) are different but there are some common characteristics to all of them. In all cases, there are two flow regimes observed, corresponding to regimes A and B described previously. Regime A corresponds to spacings where the side force is almost constant. Regime B corresponds to spacings where the side force varies rapidly.

4.10.1 Front Rod d/D = 0.17

The two sets of data points of interest in Fig.42 (Re = 3.3×10^4 and 6.5×10^4) have the same shape with a minimum side force near the critical spacing. The minimum value of Cl' was always smaller than the reference at the same Re (the reference is Cl' for the cylinder alone); the maximum reduction of Cl' is 67% for Re = 6.5×10^4 and 25% for Re = 3.3×10^4. Any spacing in regime A gave a side force reduction. In regime B, where the side force varied

rapidly, the maximum side force was not significantly larger than the reference.

Fig.45 shows the effect of rod spacing on Strouhal number for the rod d/D = 0.17; the Strouhal number increases with Reynolds number.

4.10.2 Front Rod d/D = 0.33

Fig.46 shows the effect of rod spacing on Strouhal number for $Re = 3.3 \times 10^4$. There was not a well defined dominant frequency for $Re = 6.5 \times 10^4$.

For each configuration tested at $Re = 3.3 \times 10^4$, the spectral density of the fluctuation showed two frequency peaks corresponding to the Strouhal numbers of Fig.46. The total area under the spectral density curve being proportional to $(Cl')^2$, it was assumed that the height of each frequency peak was an estimate of the contribution of that frequency to $(Cl')^2$. The contributions to $(Cl')^2$ in percentage are shown in Fig.46.

The two frequencies were assumed to be the vortex shedding frequencies of both bodies, the circular cylinder producing the low frequency and the front rod producing the high frequency.

The values of Cl' were corrected for frequency distortion using the transfer function (Fig.10) and considering the contribution of each of the two frequencies to Cl'. The result is presented in Fig.43 for $Re = 3.3 \times 10^4$. For $Re = 6.5 \times 10^4$ it was not possible to correct the data because no dominant frequencies were noticeable; these

results are plotted as if the frequency response was flat.

The trends of the two curves (Fig.43) differ significantly. This may be due to one curve not being corrected. Another possible cause of the difference is the presence of two dominant frequencies in one case. Nevertheless, the side force is relatively low, not significantly higher than the reference.

4.10.3 Front Rod d/D = 0.50

Fig.47 shows the effect of rod spacing on Strouhal number at Re = 3.3×10^4. Two dominant frequencies were noticed again, but this time the intensity due to the high frequency (front rod) was dominant as shown by the percentage values. Again at Re = 6.5×10^4 there was no dominant frequency noticeable.

The values of Cl' (Fig.44) at Re = 3.3×10^4 were corrected for frequency distortion but not the values at Re = 6.5×10^4. Again, the trends of the two curves differ significantly for the same reasons as mentioned in section 4.10.2.

The maximum Cl', obtained here in regime A, is about 50% more than the reference but the frequency is also higher. A low Cl' is useful in practice but a high frequency is also of practical use since it can prevent synchronisation of the shedding frequency with the natural frequency of the structure.

4.10.4 General Remarks

The side force results show different trends varying with Re and rod size. They also are, in some cases, the superposition of results happening at different frequencies. It is therefore difficult to draw general conclusions on the effect of the front rod on the fluctuating side force.

In all cases, the shedding frequency was increased from that of the cylinder alone. An increase in frequency or the suppression of the dominant frequency is suitable for practical purposes because it prevents the side force from matching the natural frequency of the structure.

If the device investigated here (front rod) is used primarily as a drag reduction device, it should not increase the fluctuating side force if the spacing is properly chosen and may in fact decrease it somewhat.

If the device is to be used primarily as a fluctuating side force reduction device, further investigation should be undertaken to find the optimum configuration. From the present results, it seems that the small rod d/D = 0.17 used in regime A would be the most efficient.

V. CONCLUSIONS

5.1 Conclusions

The objective of this project was to investigate the effect of placing a small rod in front of a bluff body for fluid force reduction. Two bluff bodies were studied: a flat plate and a circular cylinder. The conclusions drawn are:

(1) - Experiments on the two types of bluff body with different sizes of front rod and different Reynolds numbers always showed, at some spacing, a significant drag reduction from that of the single body. For the flat plate, a drag reduction of 36% was found for rod d/D = 0.33 at spacing L/D = 1.81 and the results were independent of Reynolds number in the range studied. For the circular cylinder a drag reduction of 58% was found for rod d/D = 0.33 at spacing L/D = 1.73 and Re = 6.5×10^4.

(2) - In all cases, two flow regimes were observed, depending on the rod spacing. The switch in flow regime occurred at a "critical" spacing, depending on the rod diameter and the Reynolds number. The minimum drag always occurred around this spacing. Regime A was observed for spacings larger than critical while regime B was observed for spacings smaller than critical. Typical values of the critical spacing were around L/D = 2.

(3) - Regime A was observed for large rod spacings. The effect of the rod consisted first, in reducing the rear body stagnation pressure by slowing down (on average) the

fluid reaching it and secondly, in creating turbulence which permitted, in the case of the circular cylinder, a better base pressure recovery. The overall effect of decreasing rod spacing in this regime was to reduce drag, especially for the circular cylinder where the drag reduction was significant mainly due to turbulence.

(4) - For smaller spacings than critical, a different flow regime (regime B) was observed; the strong interaction between the two bodies created a closed region in the gap where the pressure was essentially constant. The switch made the drag drop sharply. For smaller spacings the drag increased back again.

(5) - The drag of the front rod itself was always smaller than the drag of the same rod in a uniform flow.

(6) - In the case of the flat plate, the base pressure was essentially constant for all rod sizes and positions (regime A and B).

(7) - In the case of the circular cylinder, increasing Reynolds number reduced the overall drag due to an increase in base pressure.

(8) - An optimum rod size was determined but it changed with Re (circular cylinder only); a larger rod diameter was required for lower Re.

(9) - Yaw was found to be important for drag reduction. A yaw of 5° cancels 50% of the flat plate drag reduction in the tandem configuration.

(10) - The fluctuating side force (circular cylinder

only) was not significantly increased by the use of the front rod and was reduced in most cases. A small rod such as d/D = 0.17 seemed to be more effective for Cl' reduction than a larger rod such as d/D = 0.50. The side force reduction was better at larger spacings (regime A). The side force frequency was increased by placing a rod upstream and, for large rods, the frequency produced by the rod itself (high frequency) became very important on the cylinder. The optimum configuration for least side force (position and size of the front rod) was not precisely determined in this work.

5.2 Areas Of Further Work

(1) - A more extensive study of the fluctuating side force on the circular cylinder would precisely determine the optimum configuration for a fluctuating side force reduction device.

(2) - Many applications of this fluid force reduction device are at higher Reynolds numbers than the maximum studied here (7.0×10^4). It would therefore be useful to carry out similar experiments at higher Re, if the experimental apparatus permits.

(3) - Similar experiments should be carried out on different shapes of bluff body, such as a square cylinder.

(4) - The effect of turbulent flow instead of smooth flow should be tested.

(5) - Further work could include testing a bluff body model with two rods, one at the front and the second at the

back. A preliminary study of this model showed that adding a rod at the back (in the wake) of the present model (with front rod) did not change substantially the overall drag; the drag reduction when the two rods were located symmetrically at the critical spacing was about the same as with the front rod only. If this device is successful, it would be a bidirectional device and would find many practical applications.

BIBLIOGRAPHY

1. Every, M.J., King, R., Weaver, D.S., "Vortex-Excited Vibrations of Cylinders and Cables and Their Suppression", Ocean Engng, Vol.9, No.2, pp.135-157, 1982.

2. Morel, T., Bohn, M., "Flow Over Two Circular Disks in Tandem", J.Fluids Engng, Vol.102, March 1980.

3. Roshko, A. and Koenig, K., "Interaction Effects on the Drag of Bluff Bodies in Tandem", Proceedings of the Symposium on Aerodynamic Drag Mechanisms, Ed.G. Sovran, T. Morel and W.T. Mason, Jr., Plenum Press, New York, 1978.

4. Igarashi, T.,"Characteristics of a Flow Around Two Circular Cylinders of Different Diameters Arranged in Tandem", Bull.J.S.M.E., Vol.25, No.201, March 1982.

5. Zdravkovich, M.M. and Pridden, D.L., "Interference Between Two Circular Cylinders; Series of Unexpected Discontinuities", J.Ind.Aero., 2(1977) 255-270

6. Hiwada, M., Tagushi, T., Mabushi, I., Kumana, M., "Fluid Flow and Heat Transfer Around Two Circular Cylinders of Different Diameters in Cross Flow", Bull.J.S.M.E., Vol.22, No.167 (1979), p.715.

7. Stansby, P.K., "The Effect of End Plates on the Base Pressure Coefficient of a Circular Cylinder", Aero.J., January 1974, pp.36-37

8. Lee, B.E., "The Susceptibility of Tests on Two-Dimensional Bluff Bodies to Incident Flow Variation", J.Ind.Aero., 2(1977) 133-148

9. Stathopoulos, T., "Technique of Pneumatically Averaging Pressures", Research Report BLWT-2-1975, Faculty of Engineering Science, University of Western Ontario, London, Canada.

10. Maskell, E.C., "A Theory of Blockage Effects on Bluff Bodies and Stalled Wings in a Closed Wind Tunnel", Aero.Res.Coun. R&M 3400, 1965

11. Fage, A. and Johansen, F.C., "On the Flow of Air Behind an Inclined Flat Plate of Infinite Span", Proc.Roy.Soc.Lond., A 116, 170, 1927.

12. Parkinson, G.V., Jandali, T., "A Wake Source Model for Bluff Body Potential Flow", J.Fluid Mech. (1970), Vol.40, pp.577-594.

13. Engineering Science Data Item Number 71016, July 1973, Figure 19, Engineering Science Data Units Limited, London.

14. Townsend, A.A., 1956, The Structure of Turbulent Shear Flow, Cambridge University Press, London.

15. Achenbach, E., "Flow Past Rough Cylinders at High Re", J.Fluid Mech., Vol.46, No.2 (1971-3), p.321.

16. Engineering Science Data Item Number 70013, Figure 12, Engineering Science Data Ltd, London, 1970.

17. West, G.S. and Apelt, C.J., "The Effect of Tunnel Blockage and Aspect Ratio on the Mean Flow Past a Circular Cylinder with Reynolds Numbers between 10^4 and 10^5", J.Fluid Mech (1982), Vol.114, pp.361-377

18. Keefe, R.T., 1961, "An Investigation of the Fluctuating Forces Acting on a Stationary Circular Cylinder in a Subsonic Stream and the Associated Sound Field", Univ. Toronto Inst. Aerophys. Rep. No.76.

19. Gerrard, J.H., 1961, "An Experimental Investigation of the Oscillating Lift and Drag of a Circular Cylinder Shedding Turbulent Vortices", J.Fluid Mech., 11, 244.

20. Gerrard, J.H., 1965, "A Disturbance Sensitive Reynolds Number Range of the Flow Past a Circular Cylinder", J.Fluid Mech., Vol.22, p.187.

L/D	d/D	Cp(centre)	U_0/U_1	L/d	l_0/D
7.00	0.17	.721	.151	41.2	.436
2.32	0.17	.548	.260	13.6	.251
1.98	0.17	.516	.280	11.6	.232
1.81	0.17	.540	.290	10.6	.221
7.17	0.33	.621	.212	21.7	.615
3.15	0.33	.467	.317	9.5	.408
2.78	0.33	.431	.343	8.4	.383
2.44	0.33	.401	.367	7.4	.359
2.13	0.33	.384	.380	6.5	.335

Table I - Calculated wake velocity deficit(U_0) and characteristic wake width(l_0)

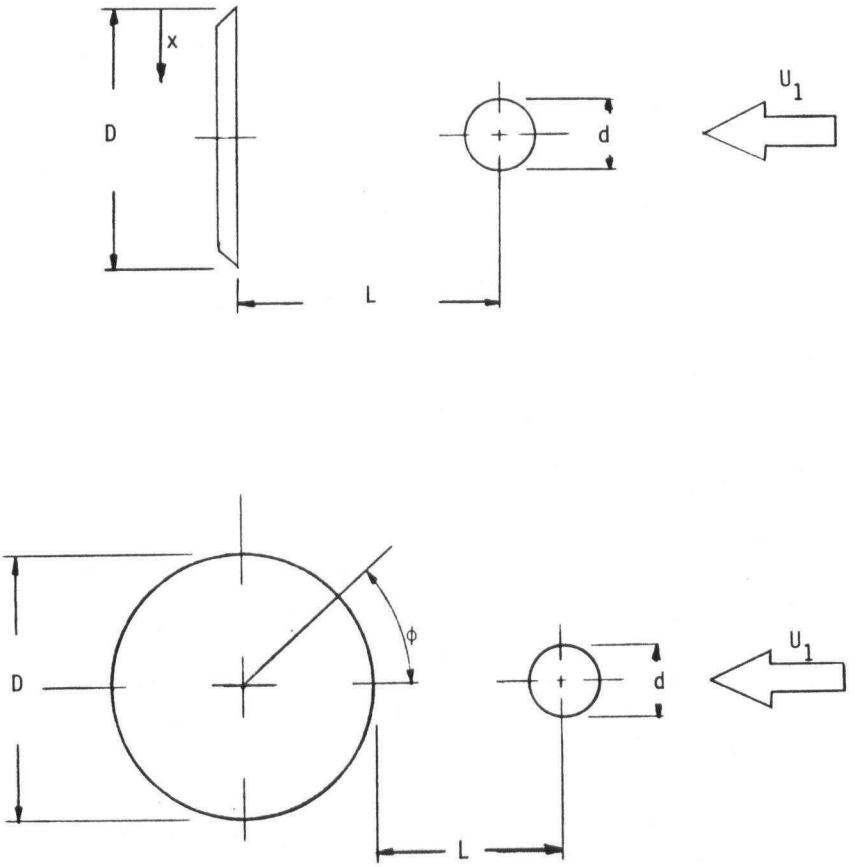

Figure 1 - Coordinate system and symbols for: (a) flat plate; (b) circular cylinder

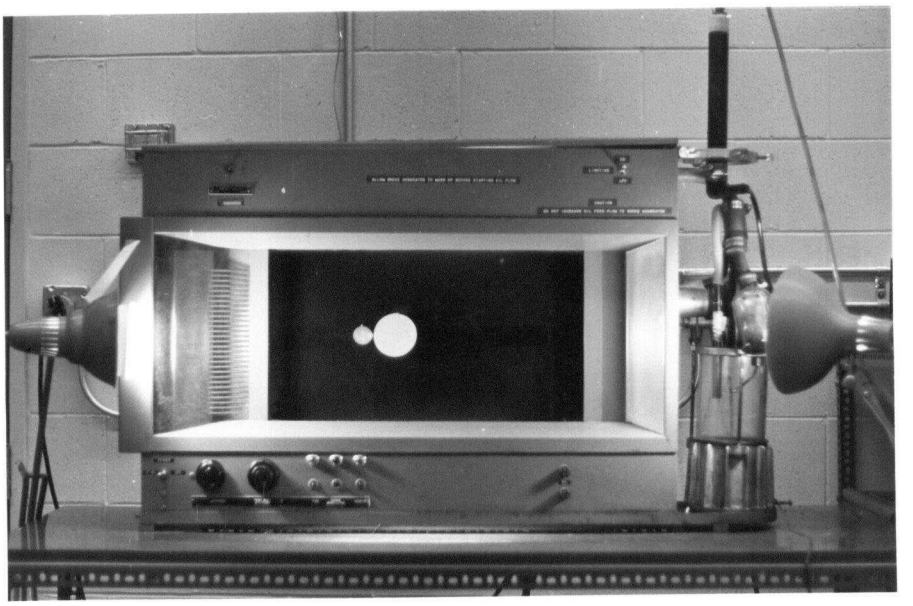

Figure 2 - Smoke tunnel

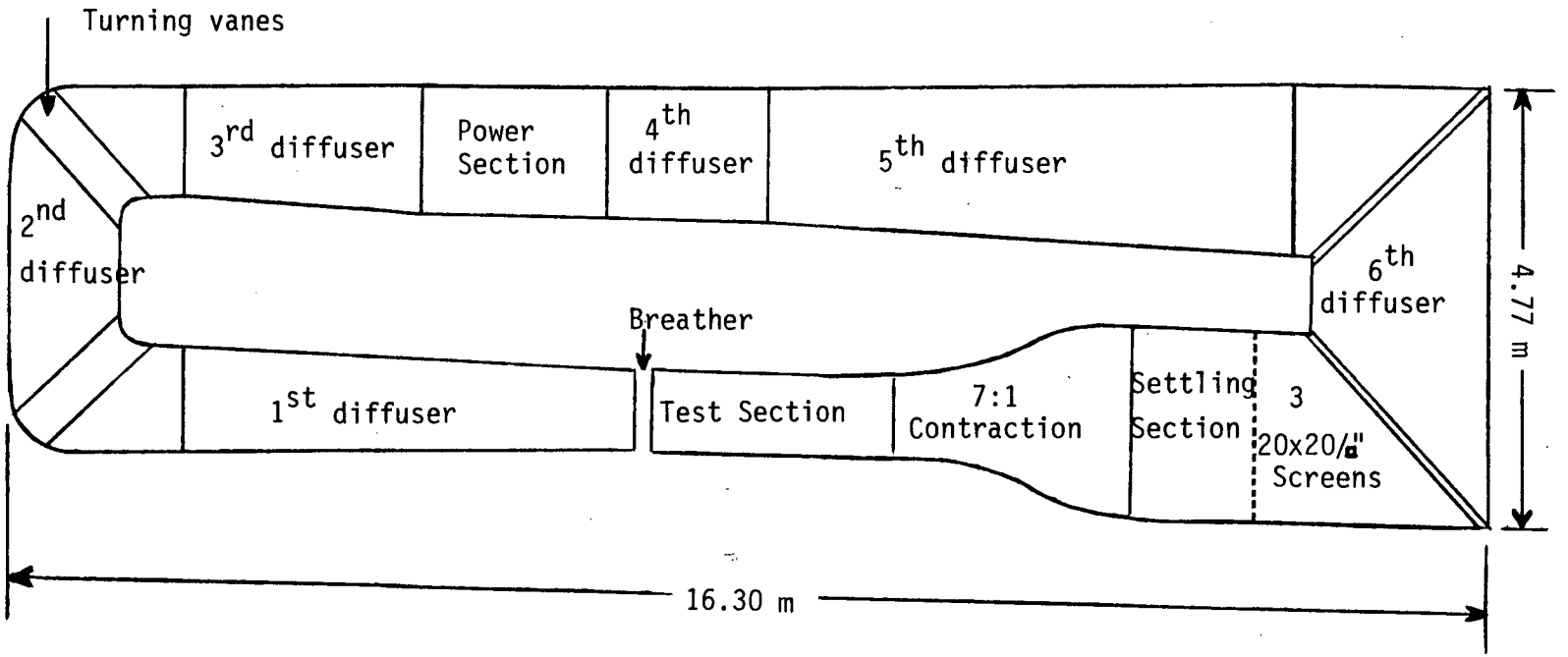

Figure 3 - Outline of the U.B.C. aeronautical wind tunnel

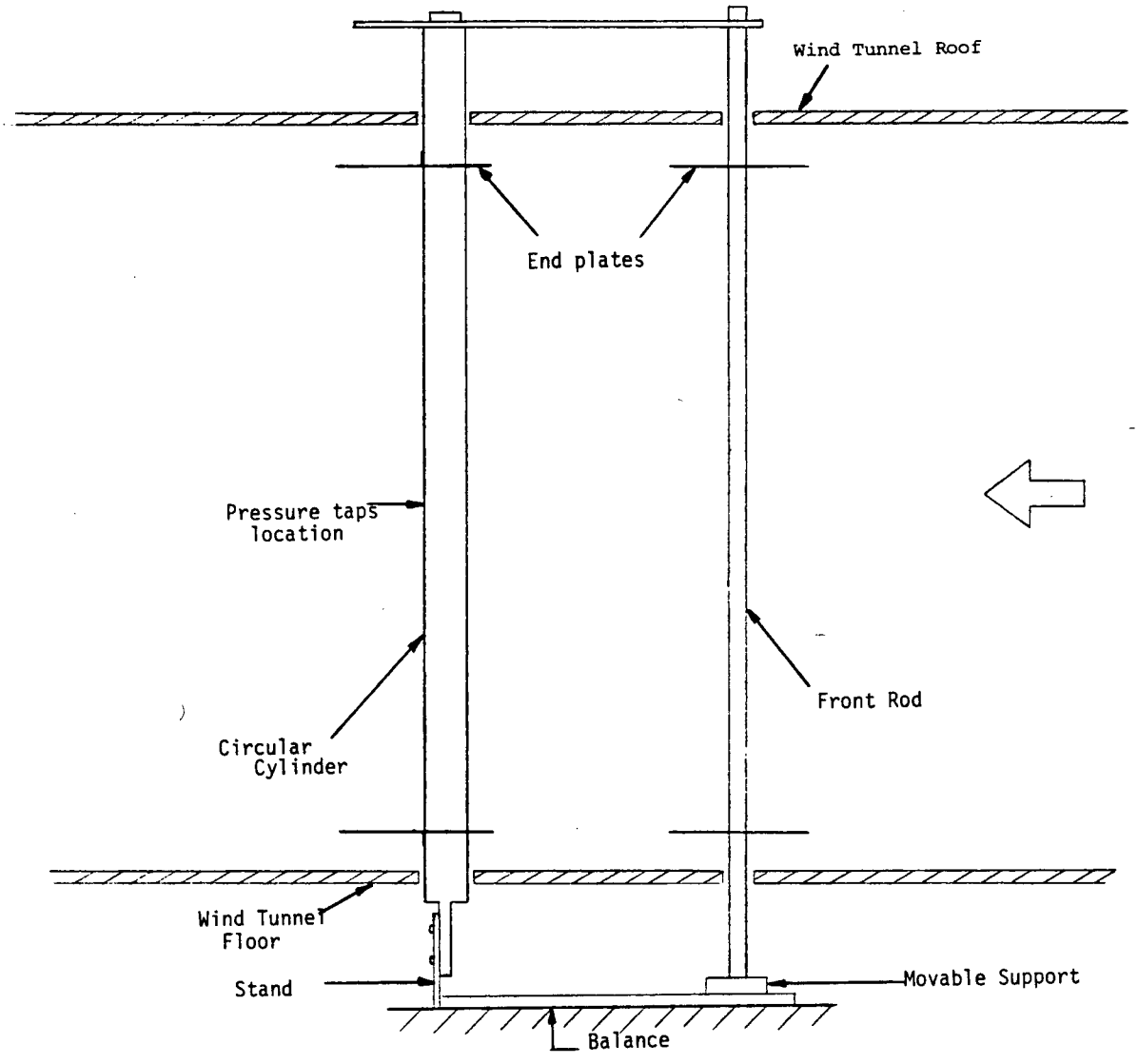

Figure 4 - Sketch of a typical model inside the wind tunnel

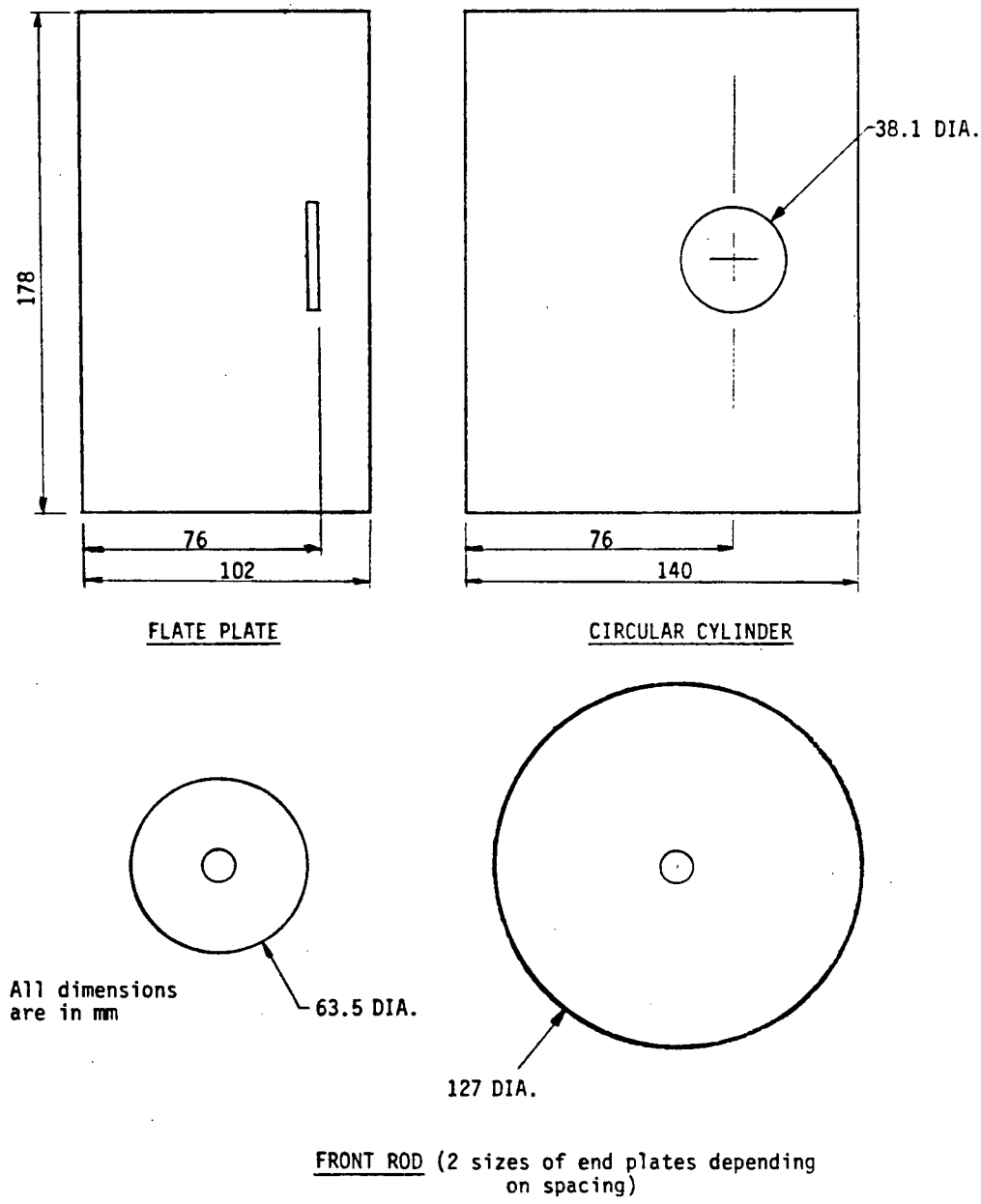

Figure 5 - End plates

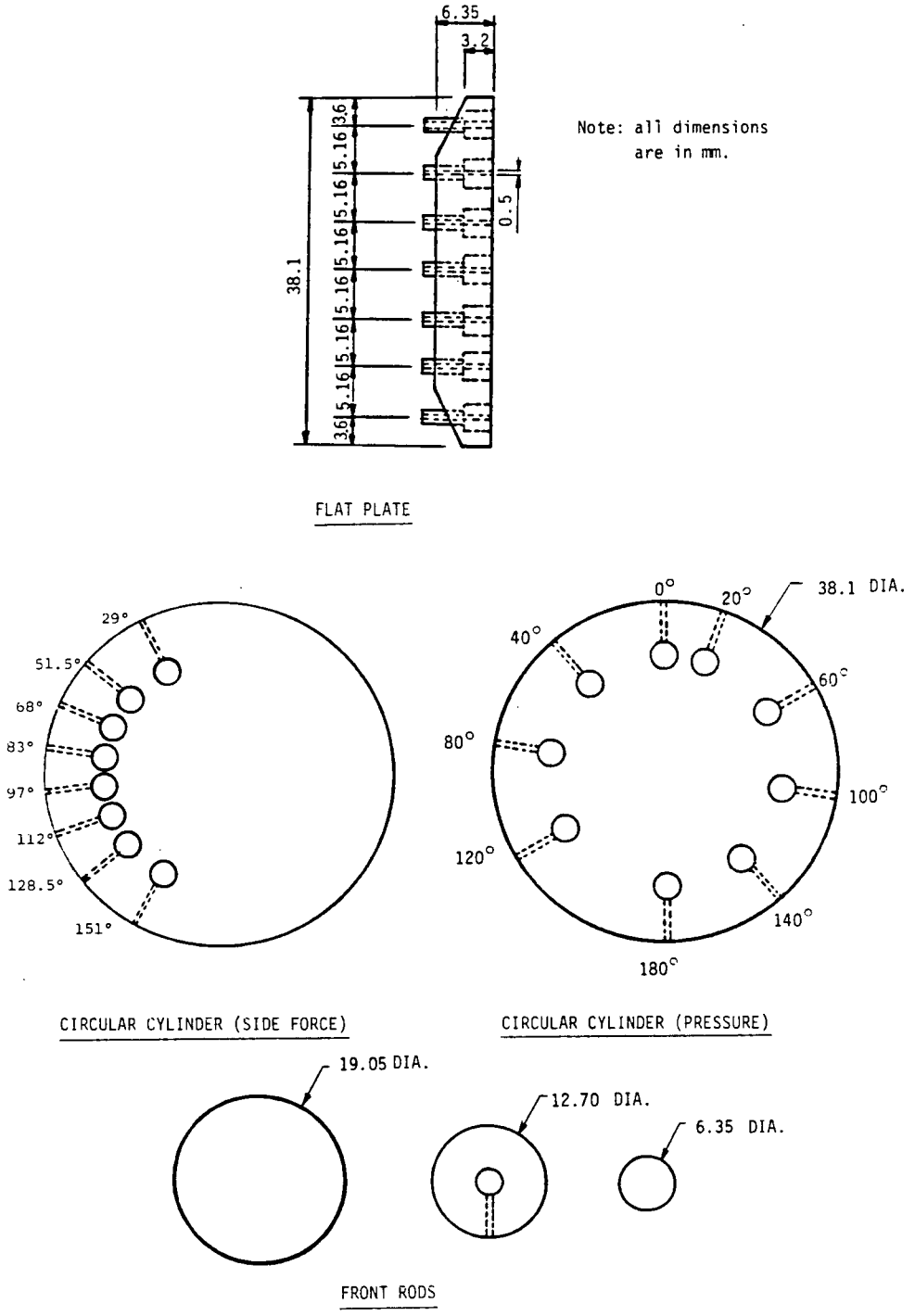

Figure 6 - Cross section of models showing pressure tap location

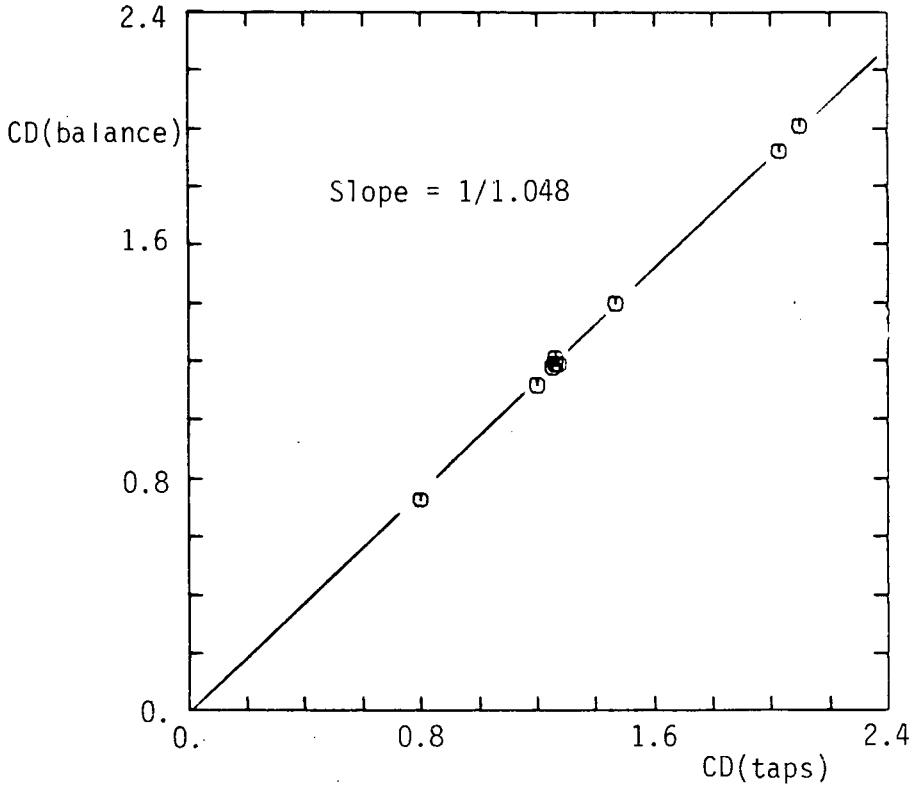

Figure 7 - Balance calibration curve

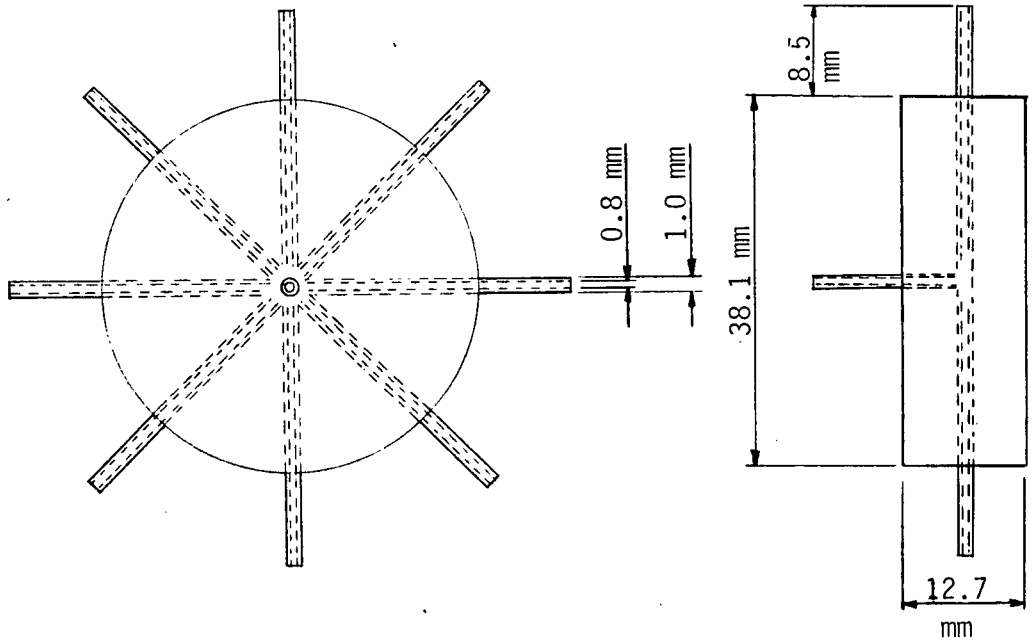

Figure 8 - Sketch of manifold for pneumatic averaging

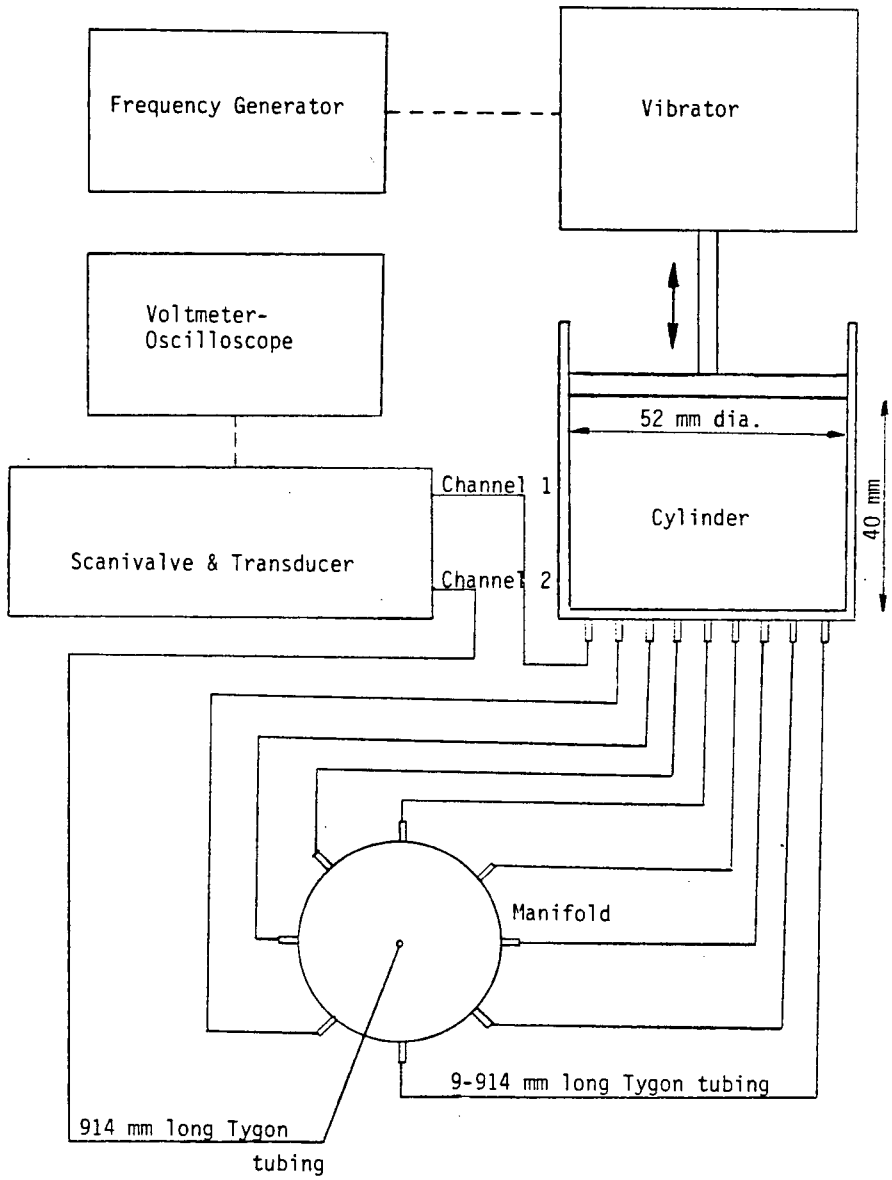

Figure 9 - Apparatus for calibration of the side force measuring system against frequency distortion

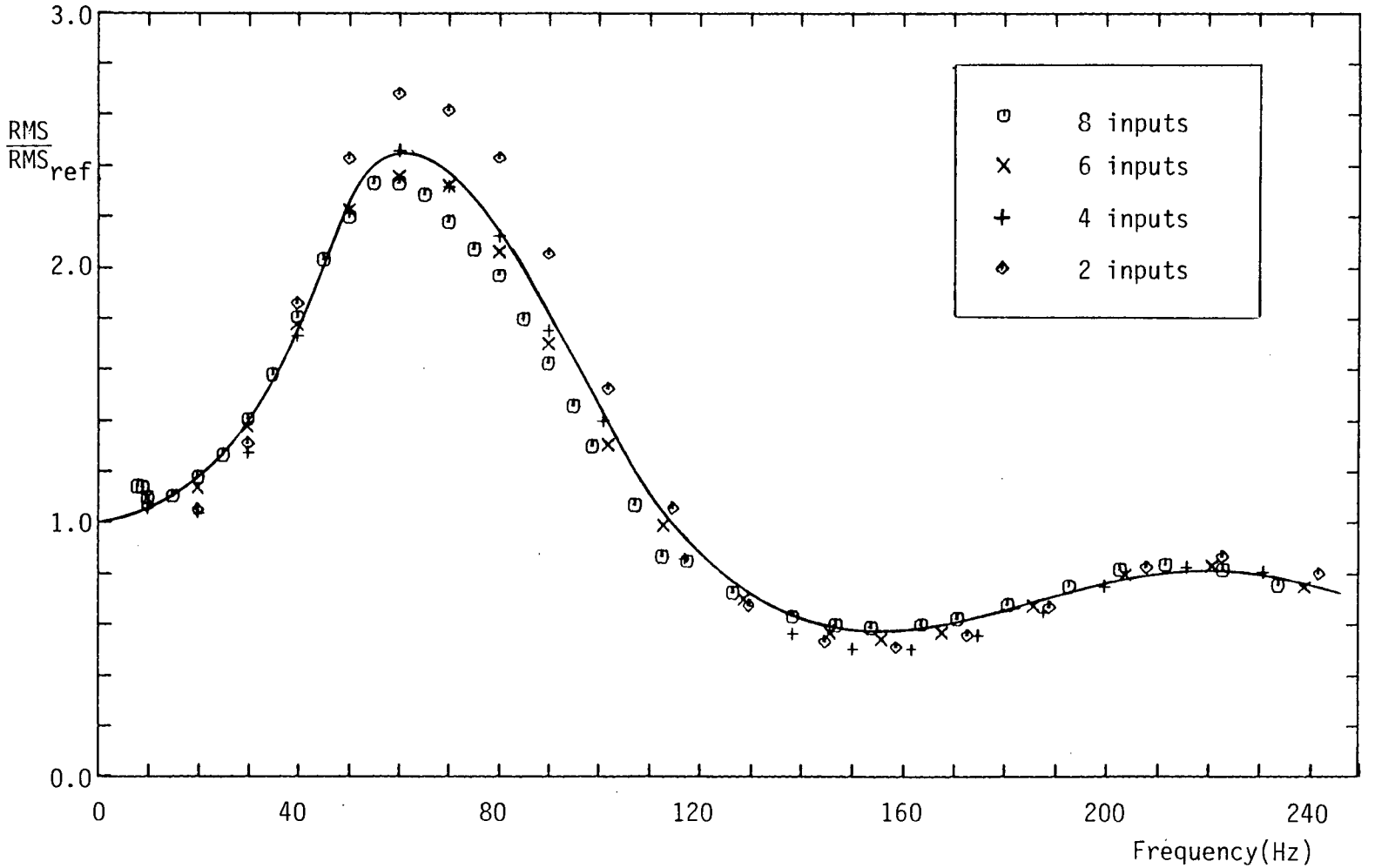

Figure 10 - Transfer function for the side force measuring system. The solid line was used to correct data

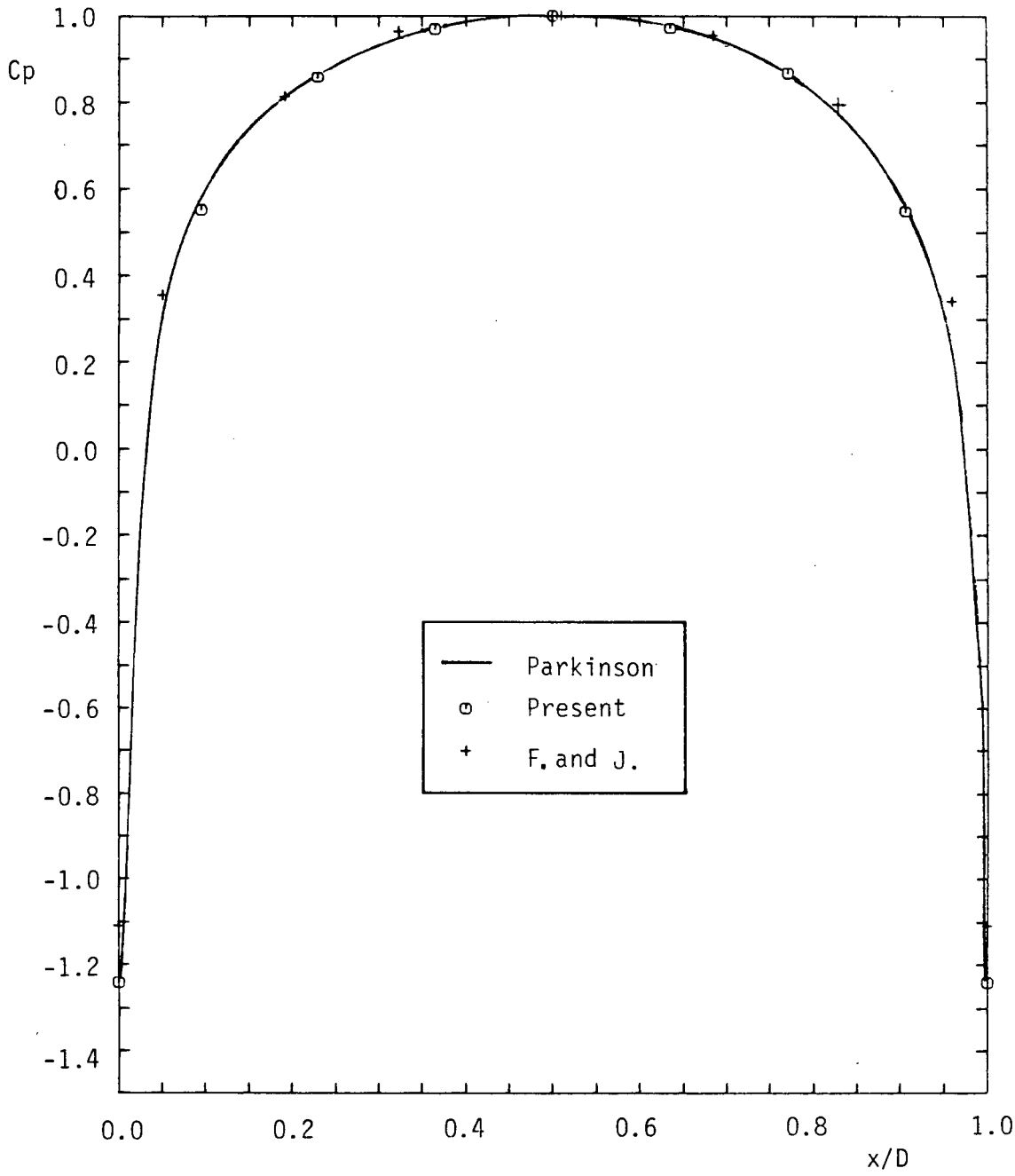

Figure 11 - Pressure distribution on flat plate ($Re=4.0x10^4$)

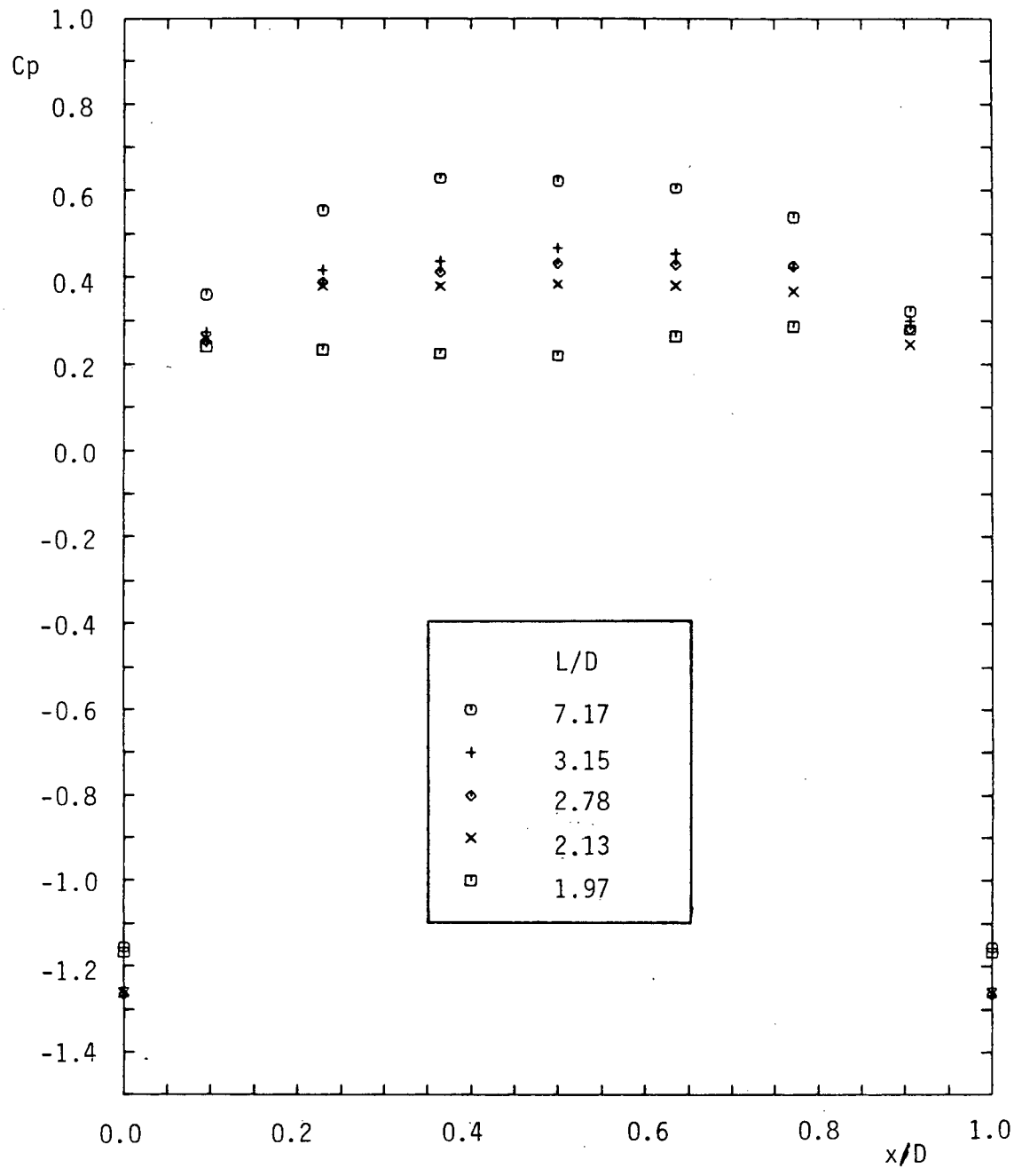

Figure 12 - Pressure distribution on flat plate with front rod d/D = 0.33 ($Re=4.0x10^4$); Flow regime A

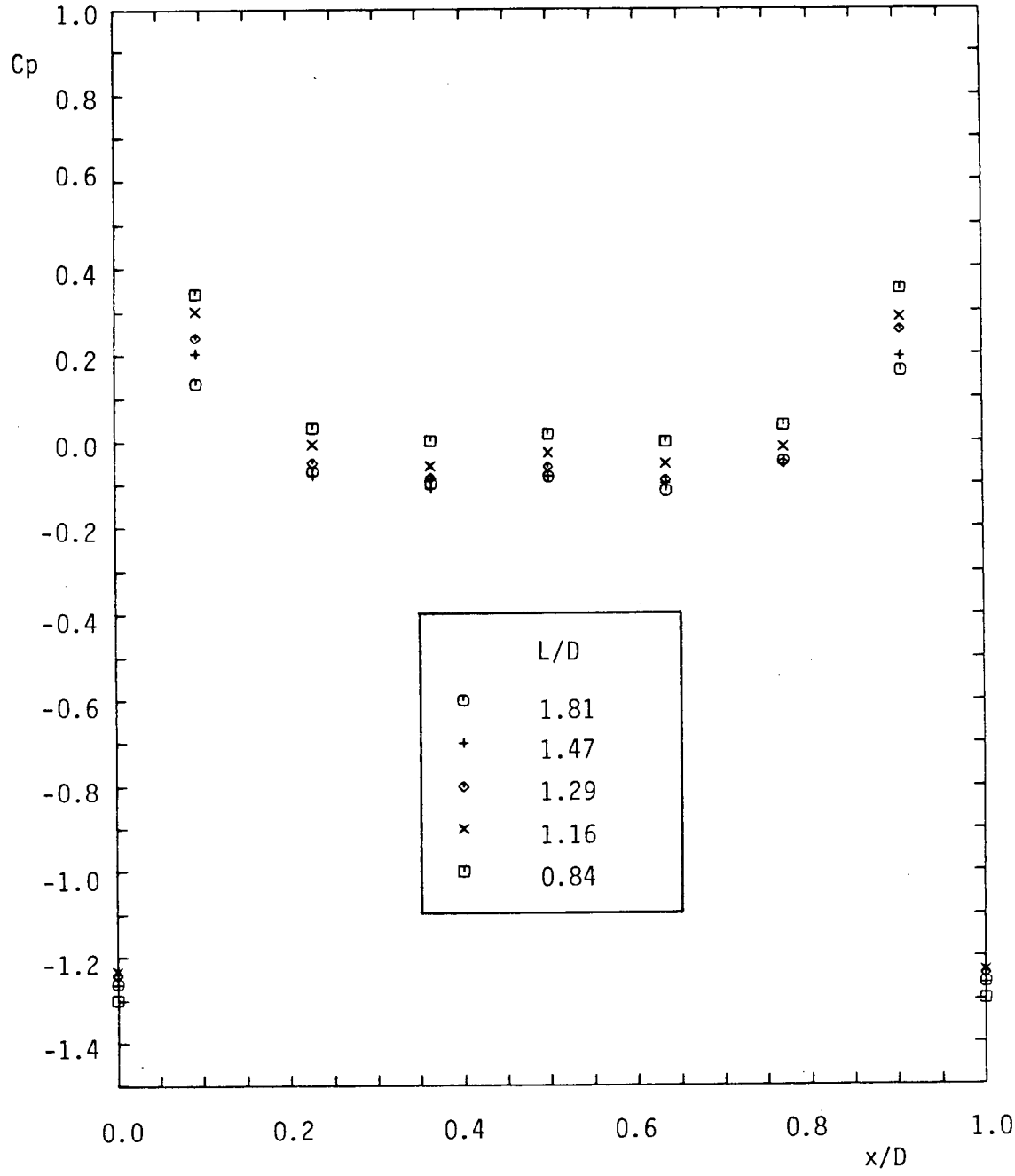

Figure 13 - Pressure distribution on flat plate with front rod d/D = 0.33 ($Re=4.0 \times 10^4$); Flow regime B

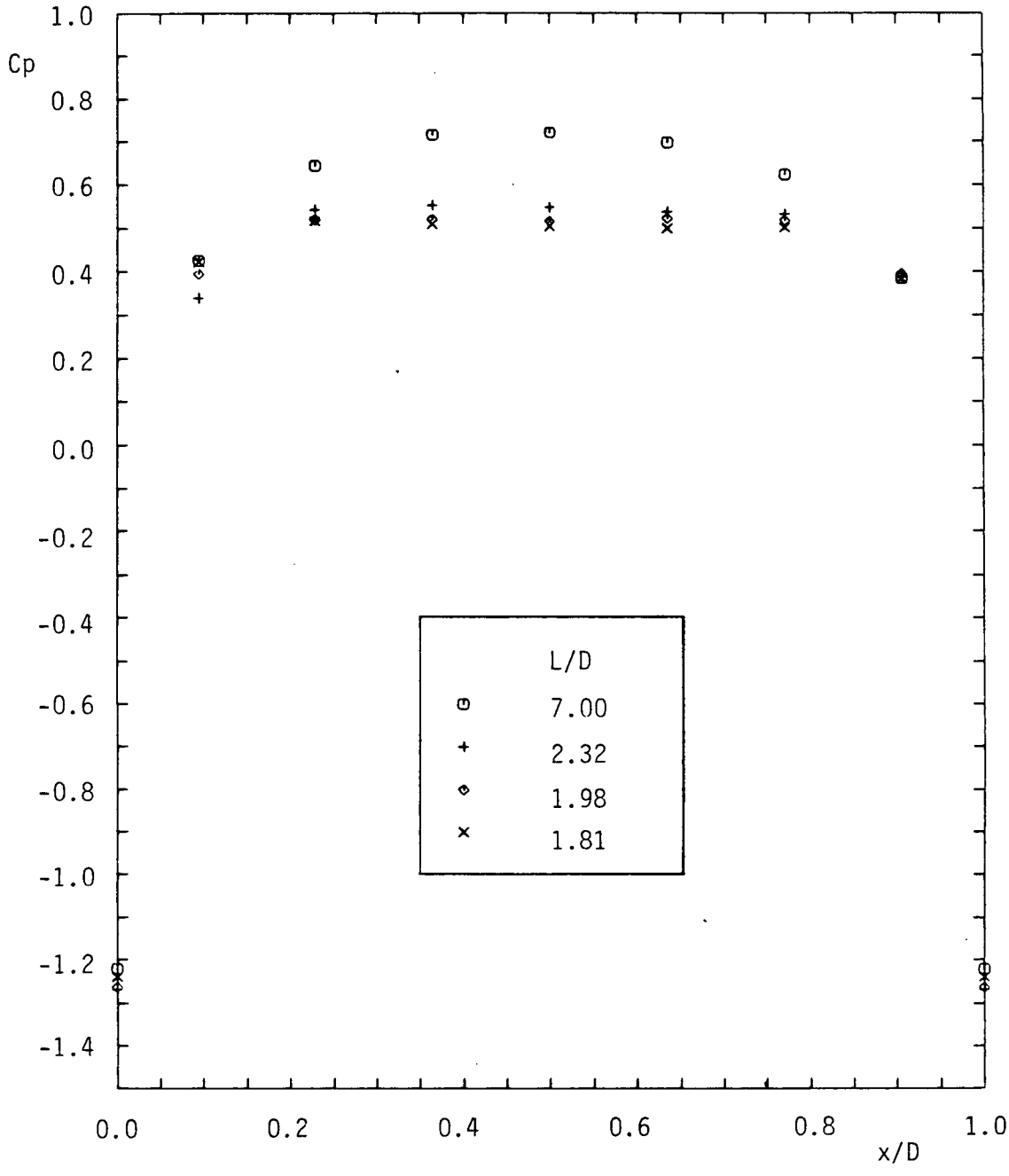

Figure 14 - Pressure distribution on flat plate with front rod d/D = 0.17 ($Re=4.0 \times 10^4$); Flow regime A

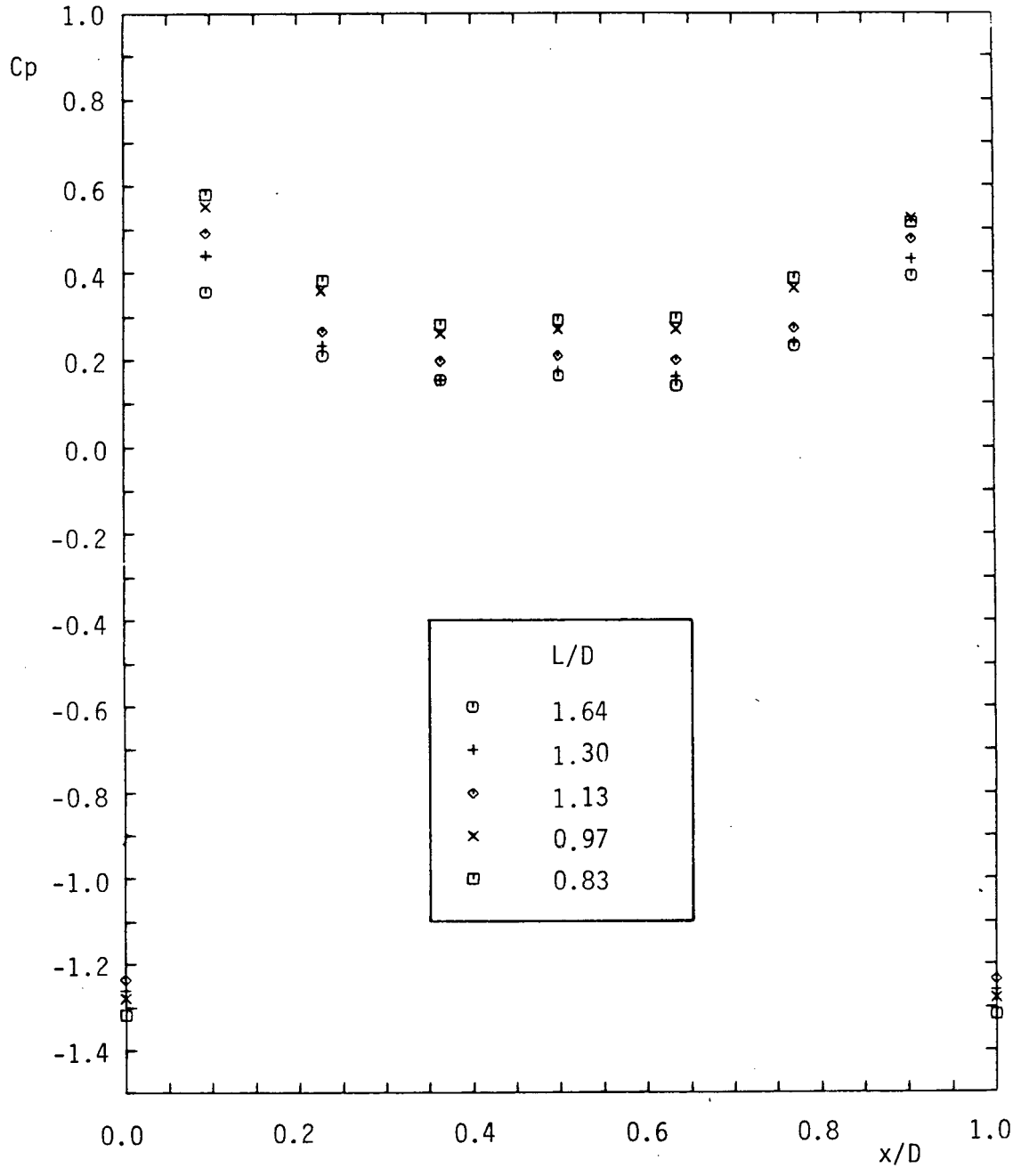

Figure 15 - Pressure distribution on flat plate with front rod d/D = 0.17 ($Re=4.0\times10^4$); Flow regime B

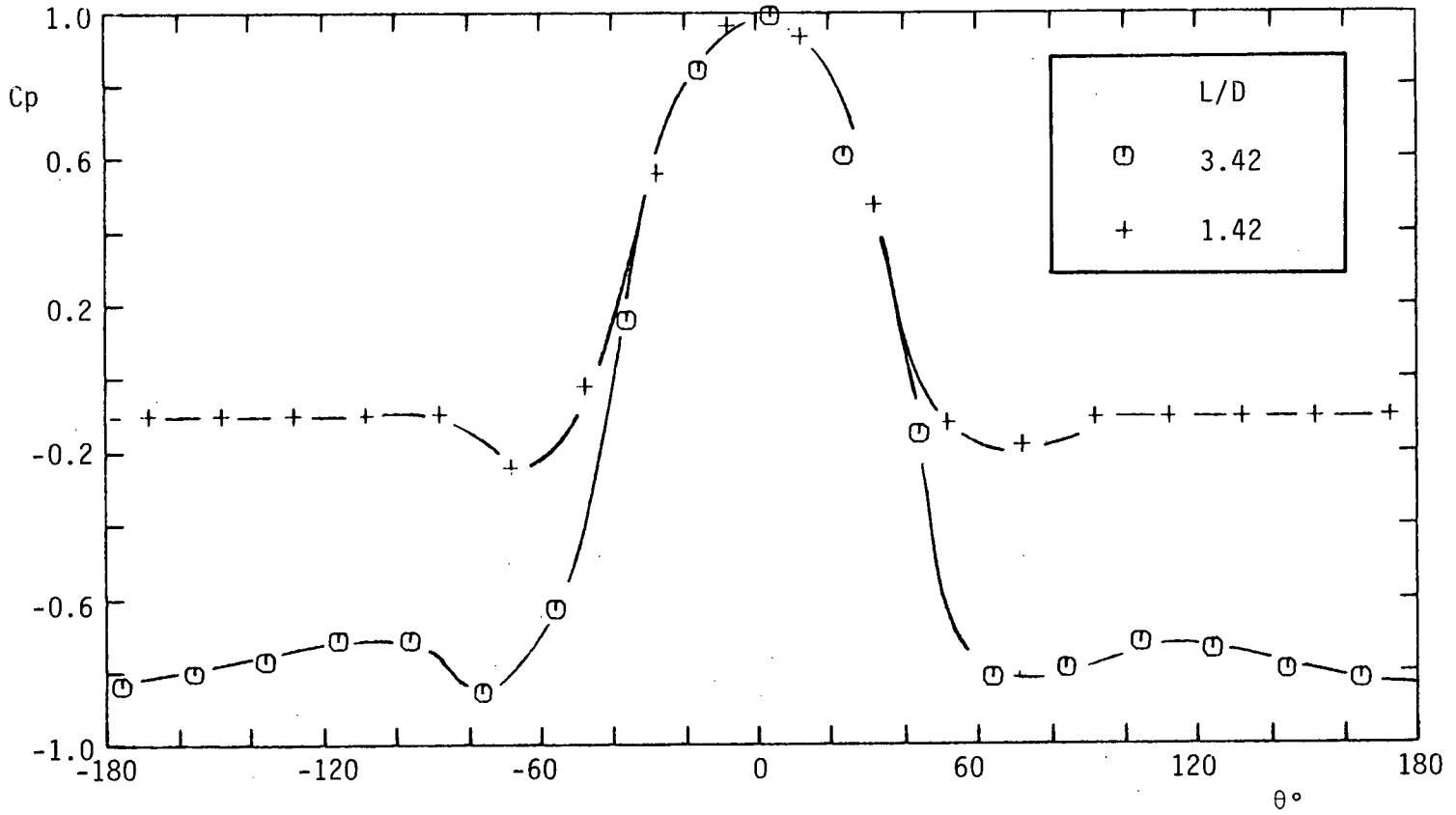

Figure 16 - Pressure distribution on the front rod d/D = 0.33 at two different spacings (Re=5.0x10⁴); L/D = 3.42 (regime A) and L/D = 1.42 (regime B)

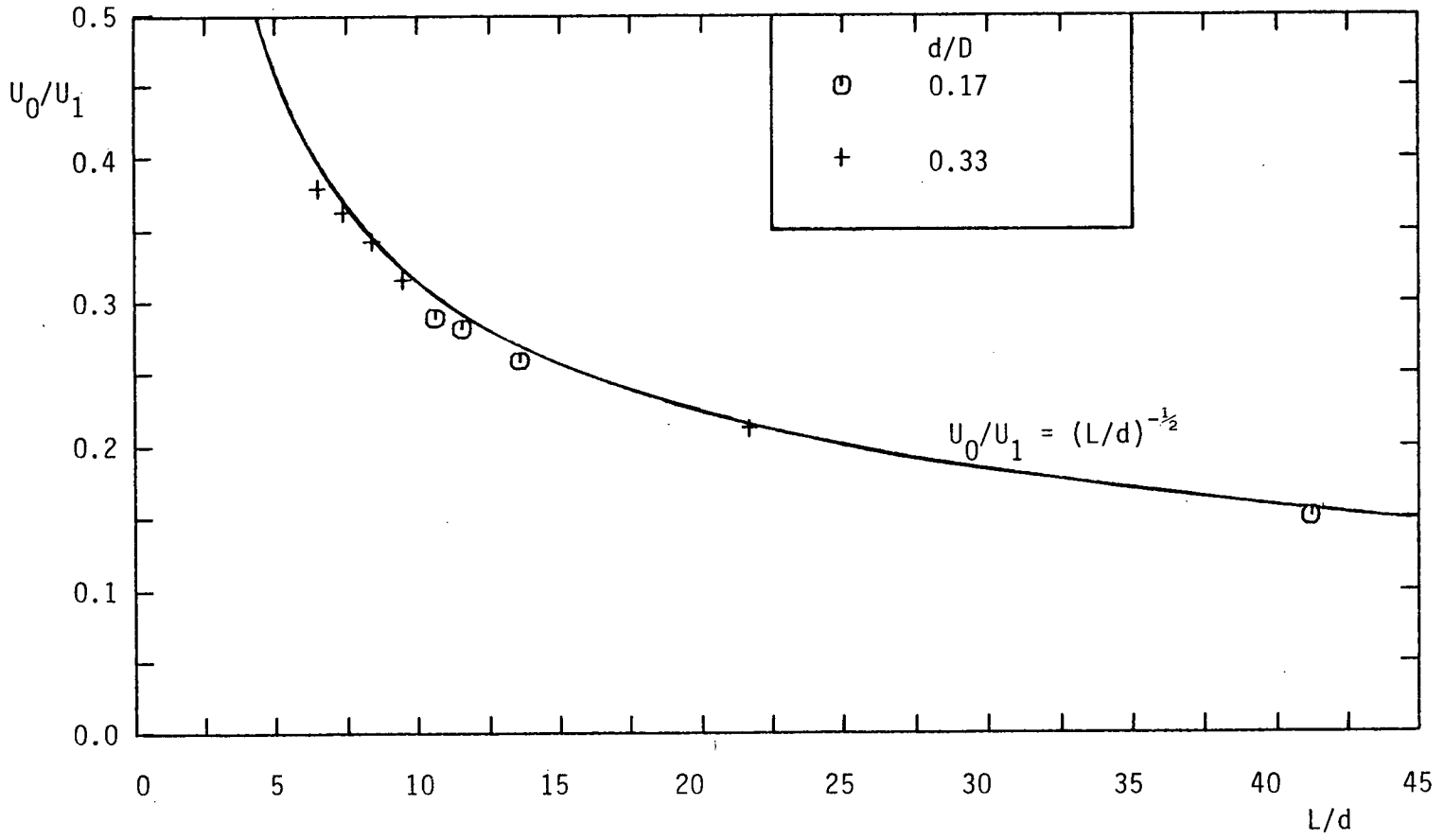

Figure 17 - Velocity deficit (U_0) versus spacing (L/d) for flow regime A

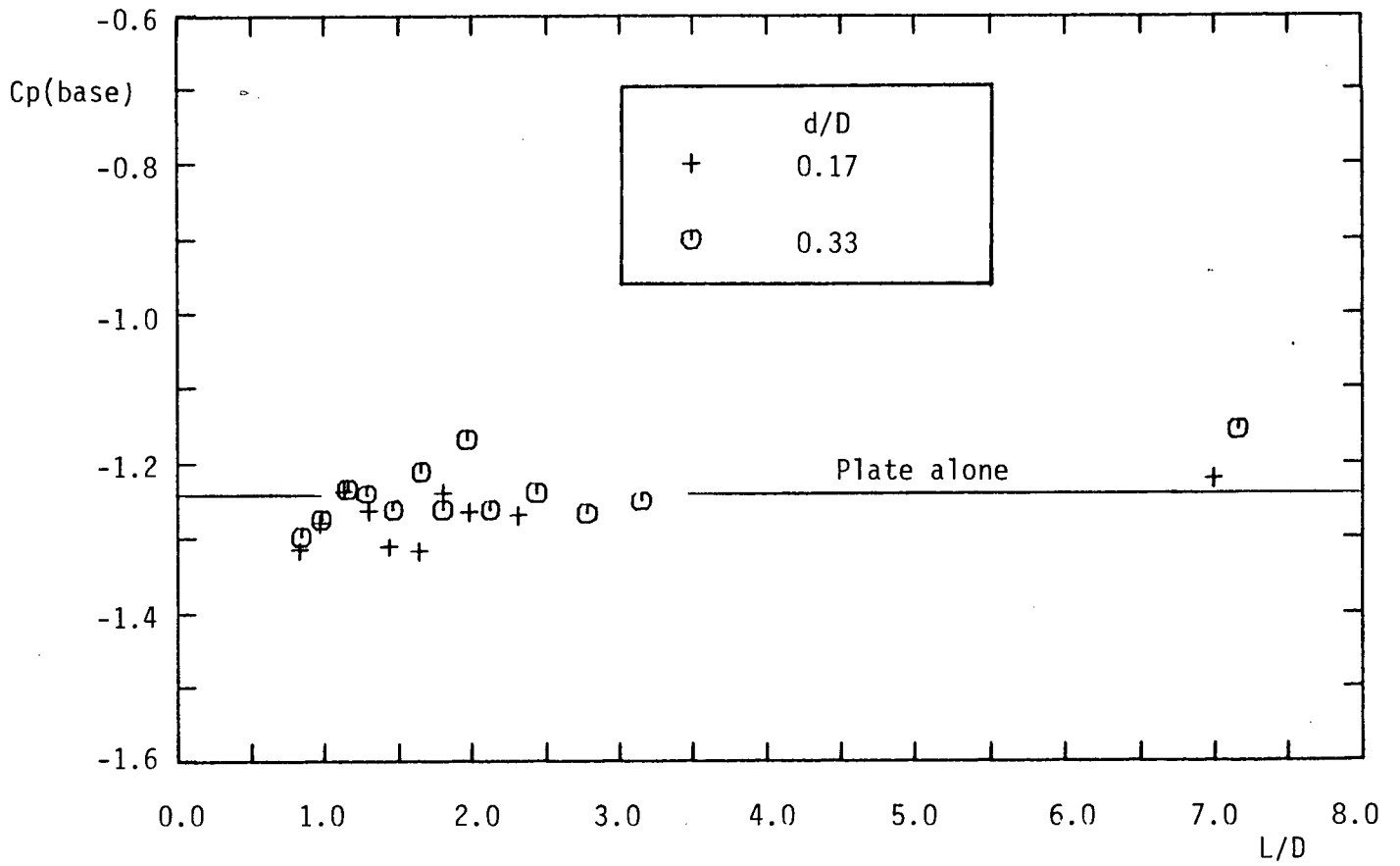

Figure 18 - Base pressure for regimes A and B

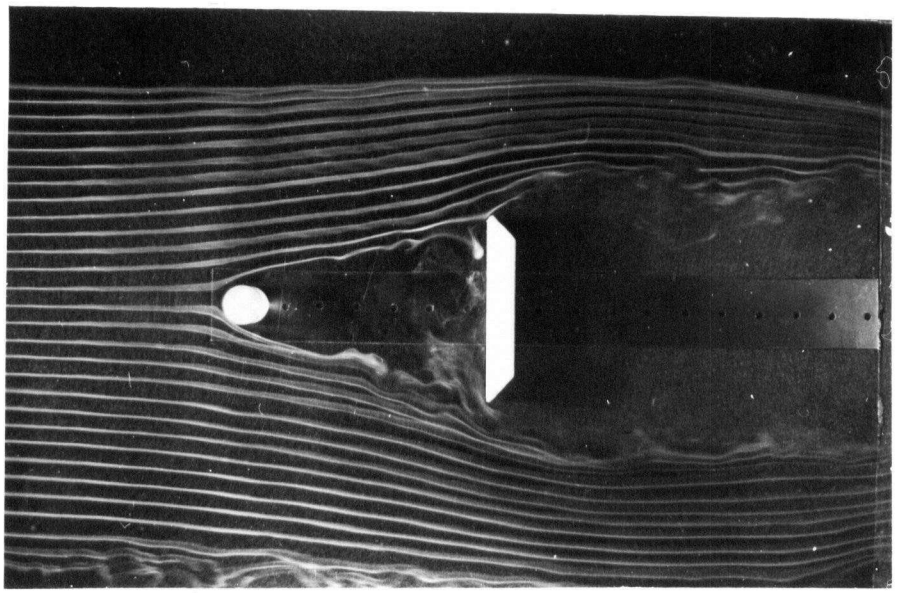

(a)

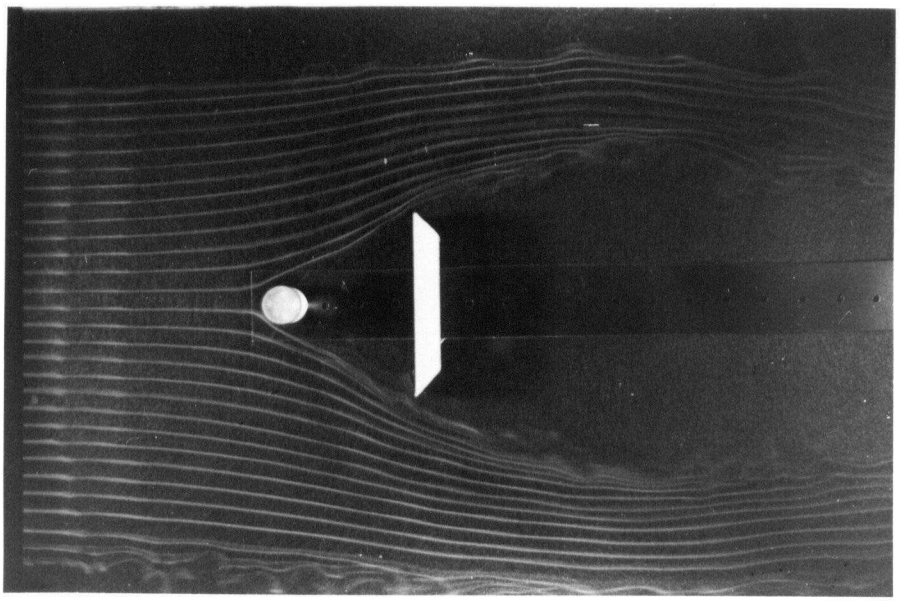

(b)

Figure 19 - Flow visualisation at Re = 5×10^3 for front rod d/D = 0.21; (a) L/D = 1.36 (regime A); (b) L/D = 0.79 (regime B)

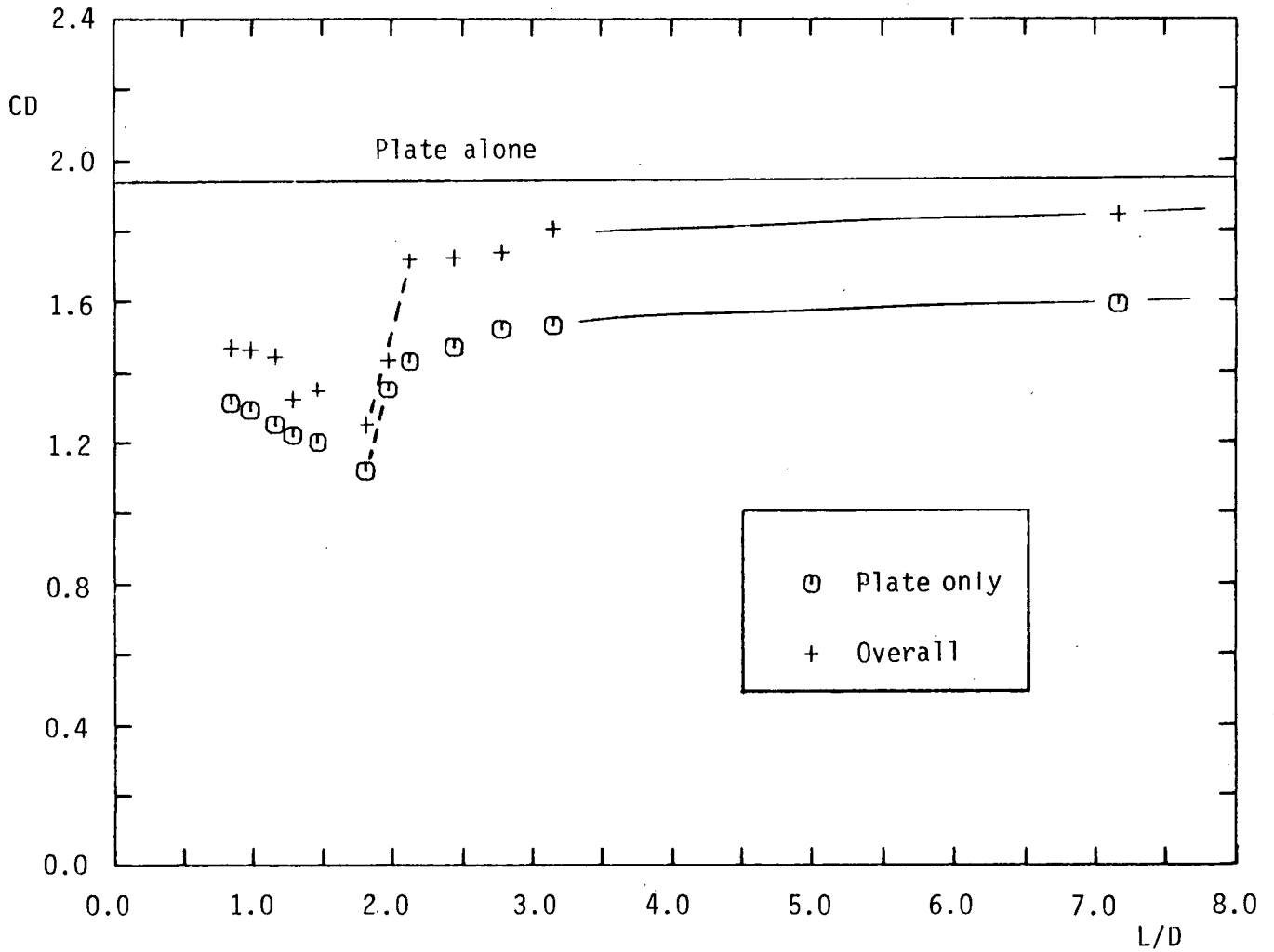

Figure 20 - Drag coefficient of flat plate with rod
d/D = 0.33 ($Re=4.0x10^4$)

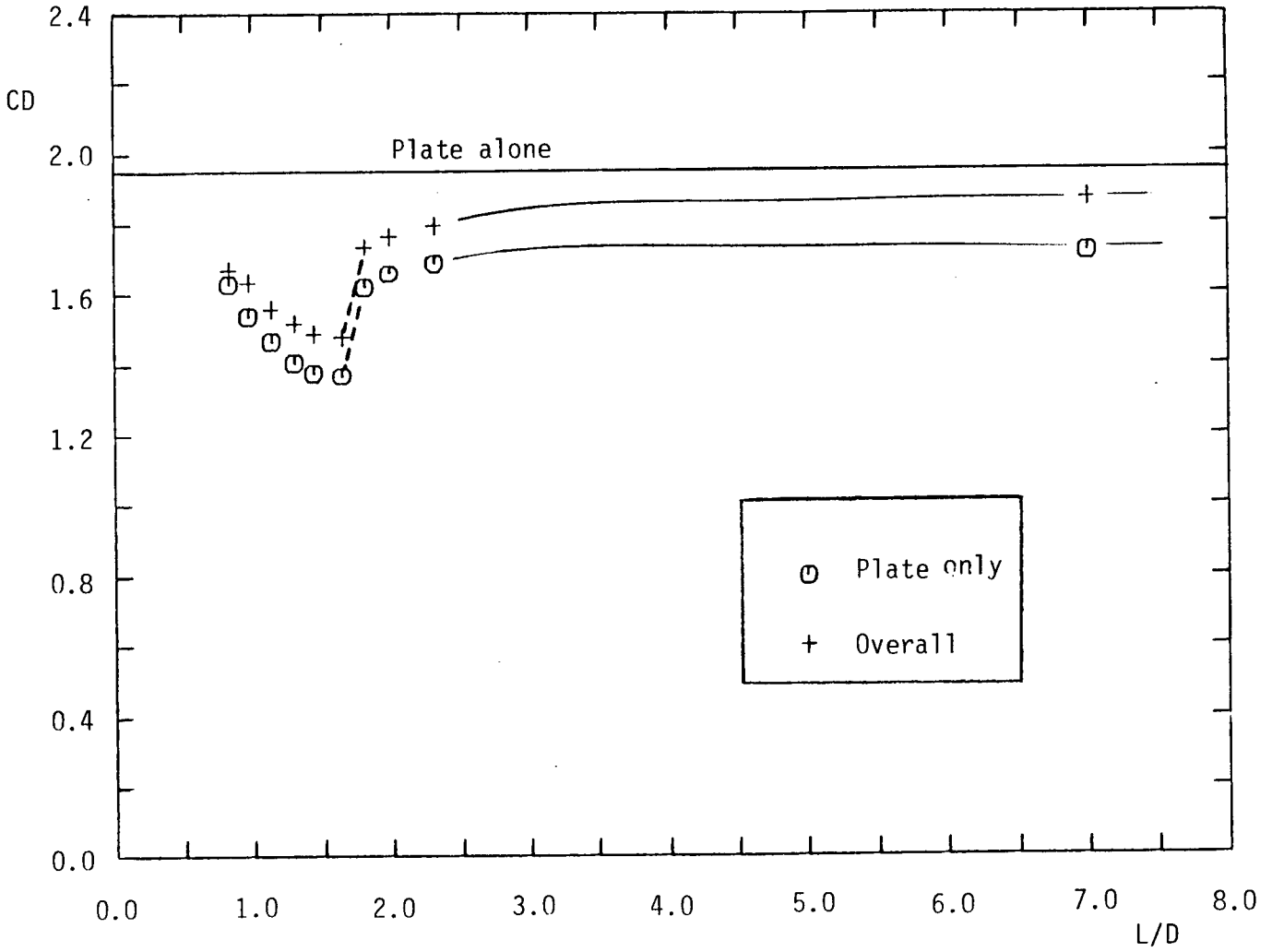

Figure 21 - Drag coefficient of flat plate with rod
d/D = 0.17 (Re=4.0x10^4)

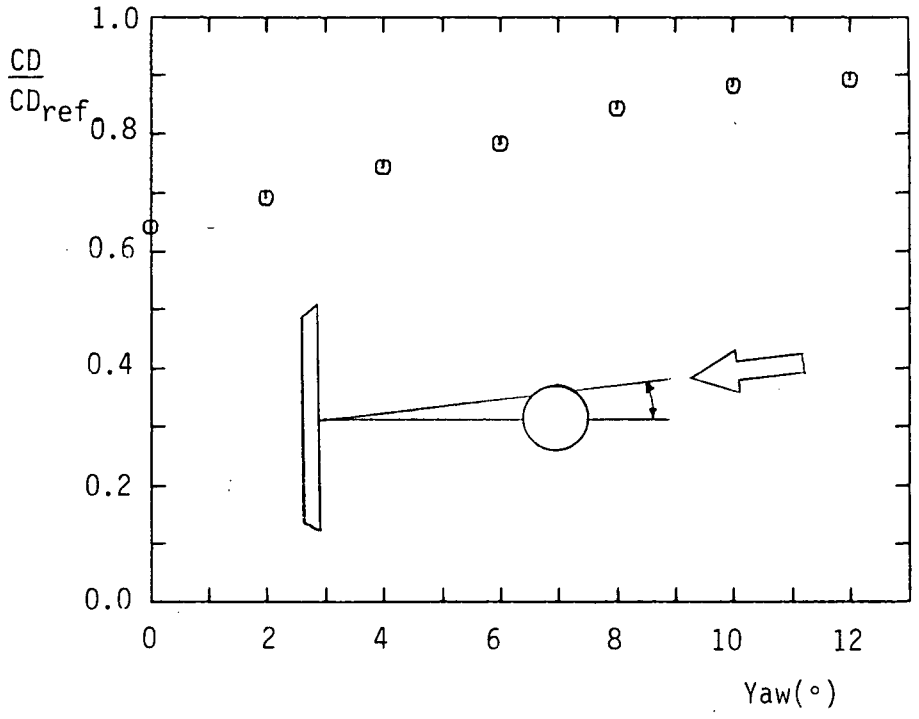

Figure 22 - Effect of yaw on the overall drag (plate and rod) for rod d/D = 0.33 at L/D = 1.42 ($Re=5.0x10^4$)

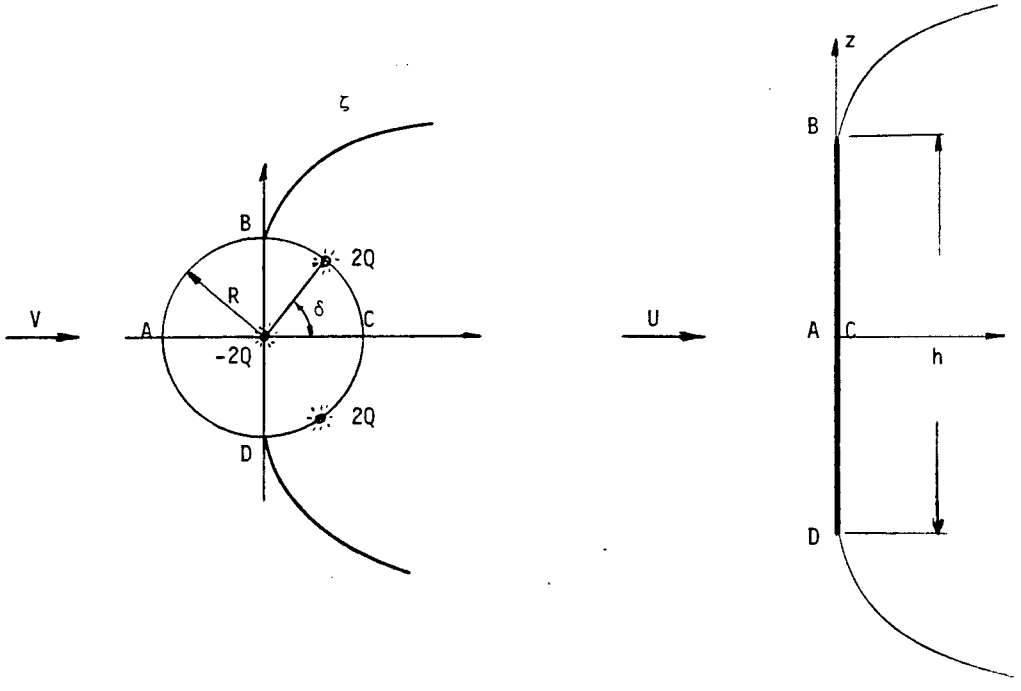

Figure 23 - Separated flow past a normal flat plate from wake source model

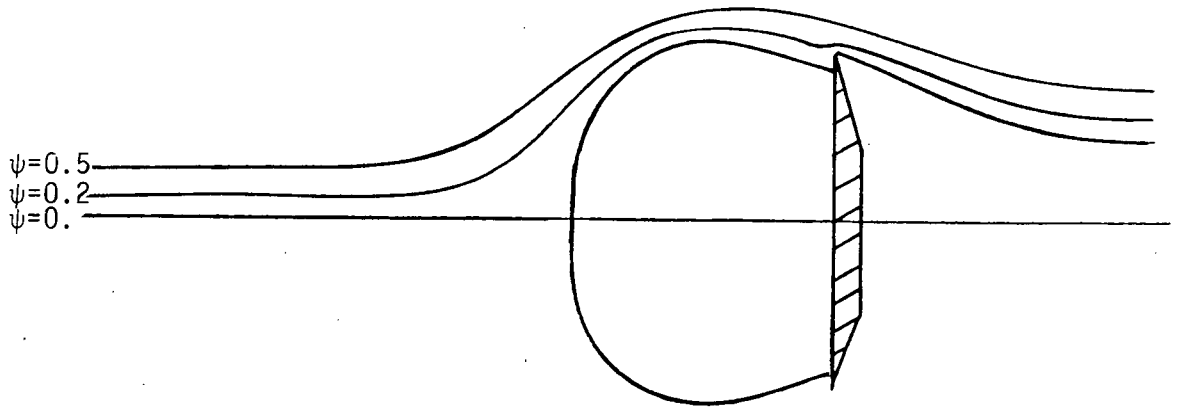

Figure 24 - Streamlines over potential model using condition for stationary pair of vortices; Cpb = - 1.24

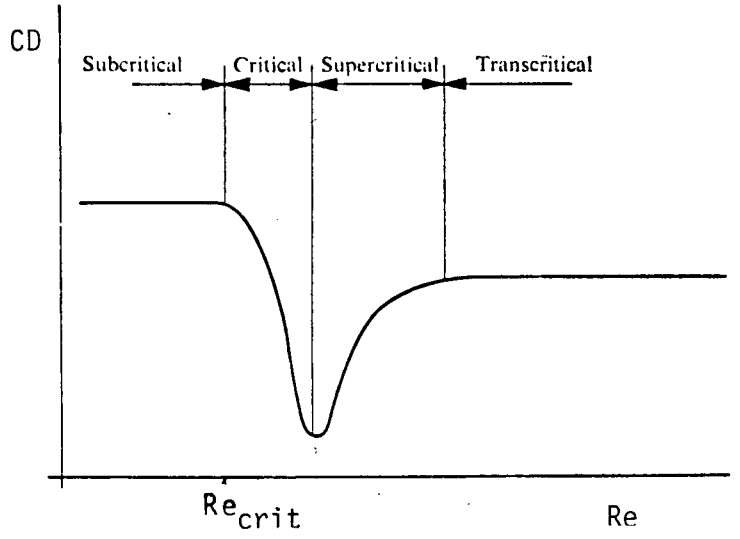

Figure 25 - Typical drag coefficient versus Reynolds number from Achenbach

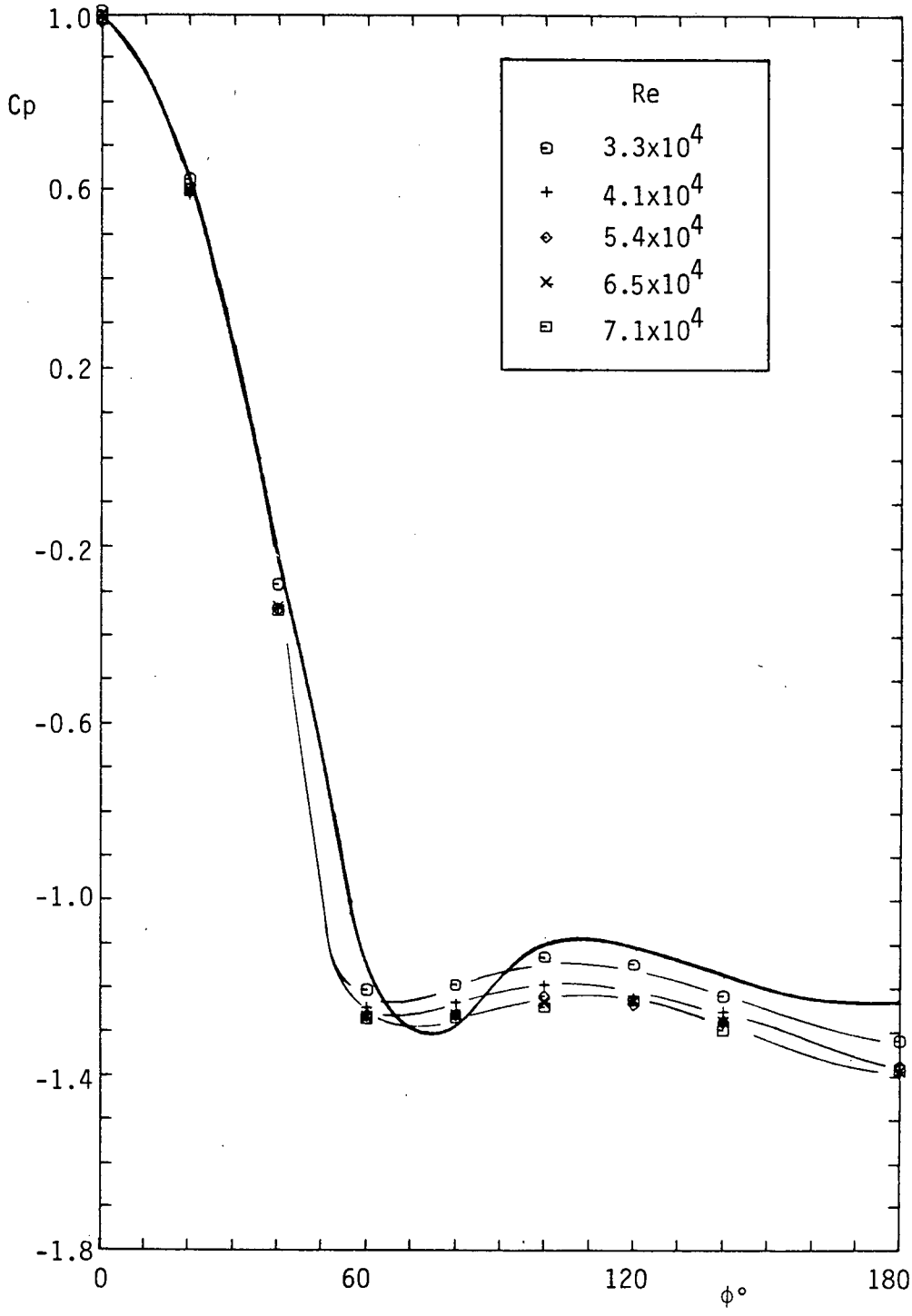

Figure 26 - Pressure distribution around a circular cylinder at various Reynolds numbers; solid line is from ESDU for subcritical range

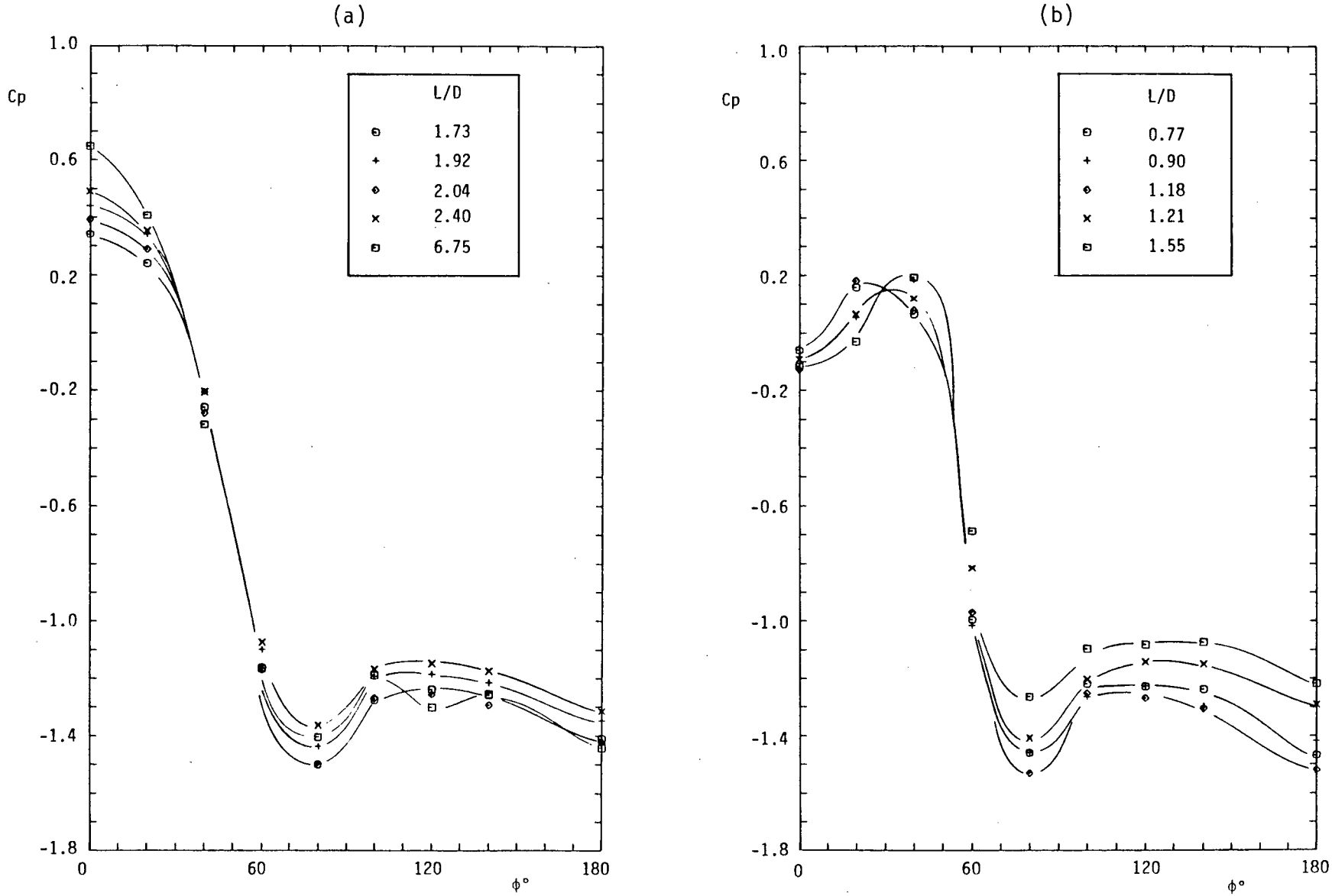

Figure 27 - Pressure distribution around a circular cylinder at Re = 1.0×10^4 with front rod d/D = 0.17. (a) regime A; (b) regime B

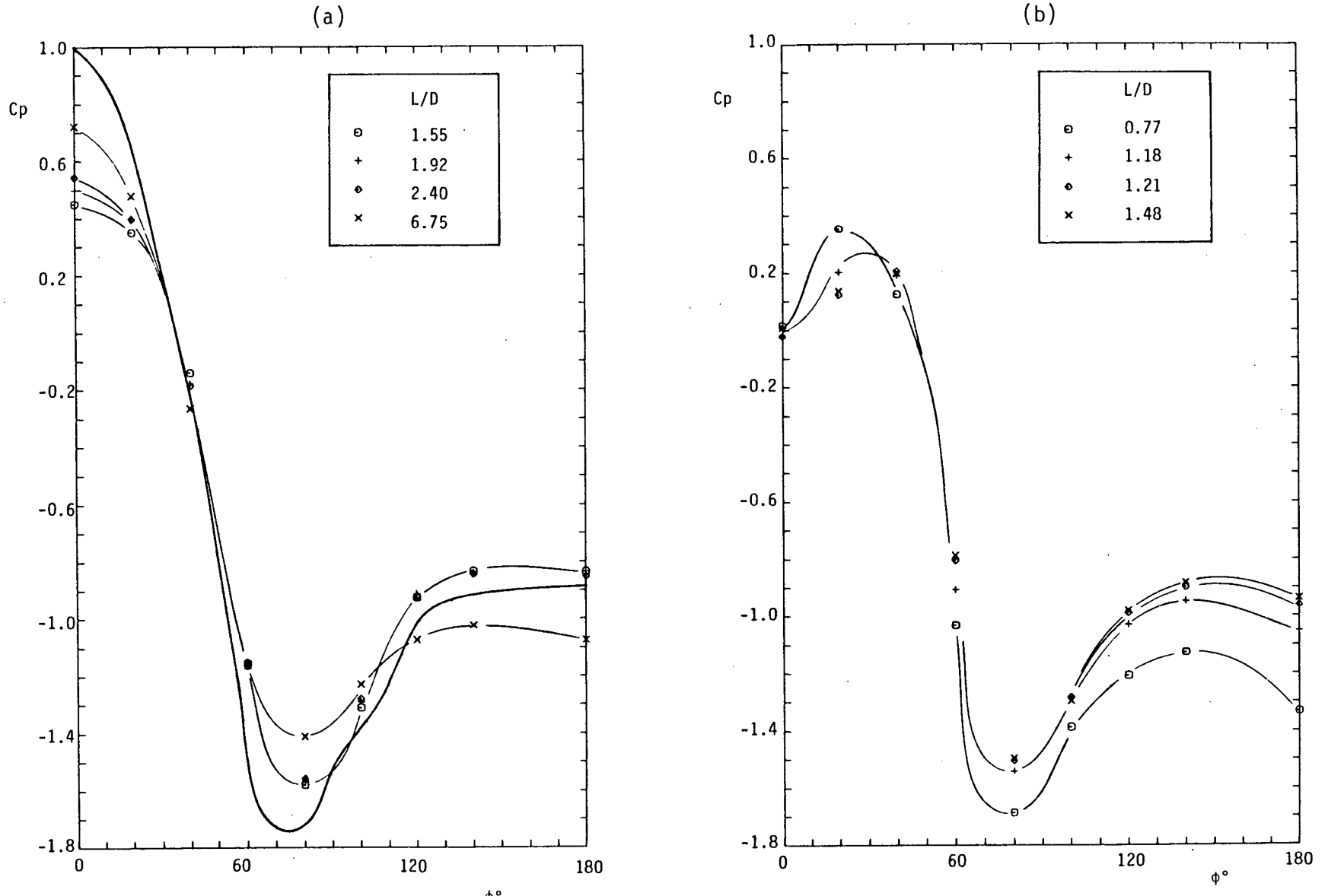

Figure 28 - Pressure distribution around a circular cylinder at Re = 3.3×10^4 with front rod d/D = 0.17. (a) regime A; (b) regime B

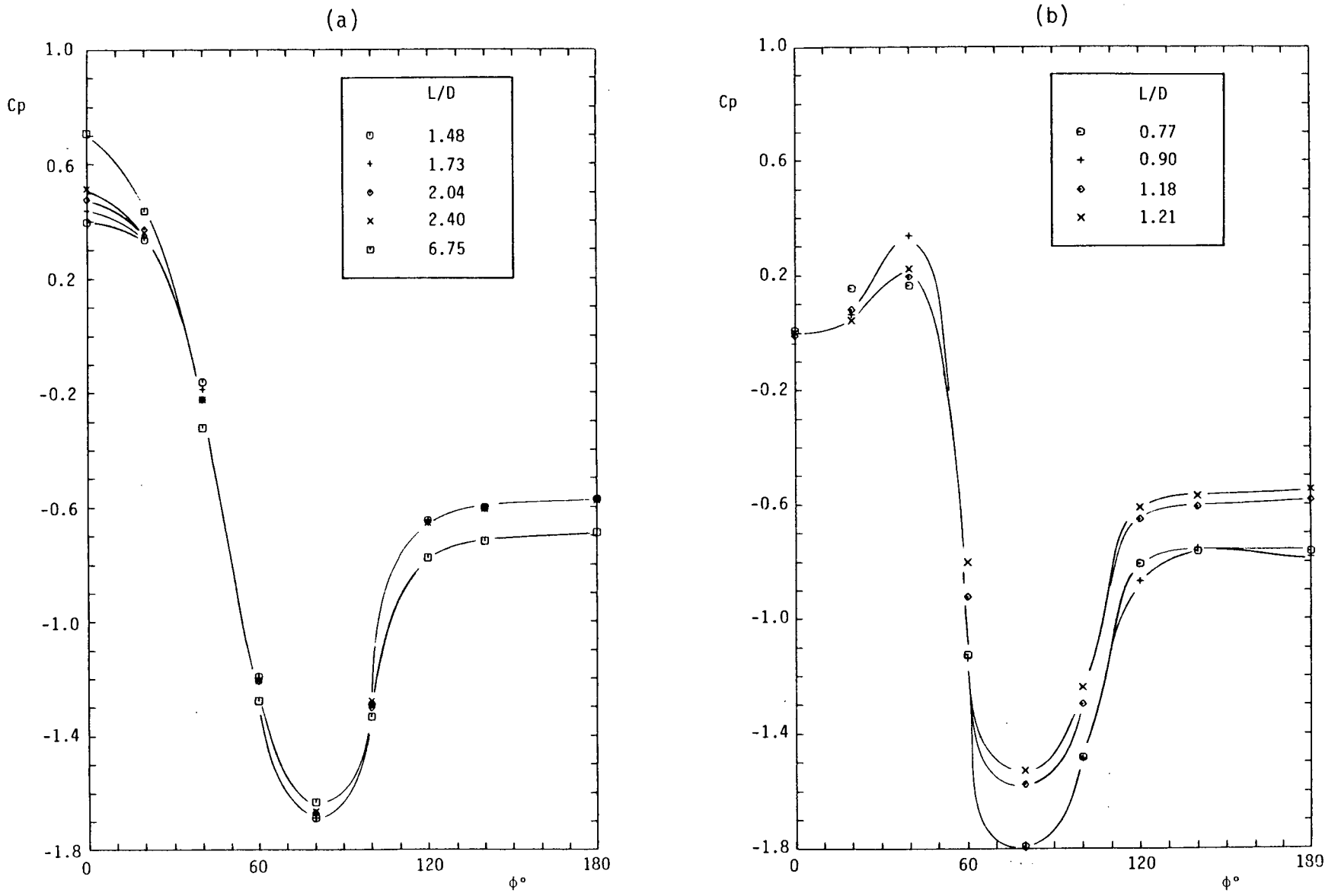

Figure 29 - Pressure distribution around a circular cylinder at Re = 6.5×10^4 with front rod d/D = 0.17. (a) regime A; (b) regime B

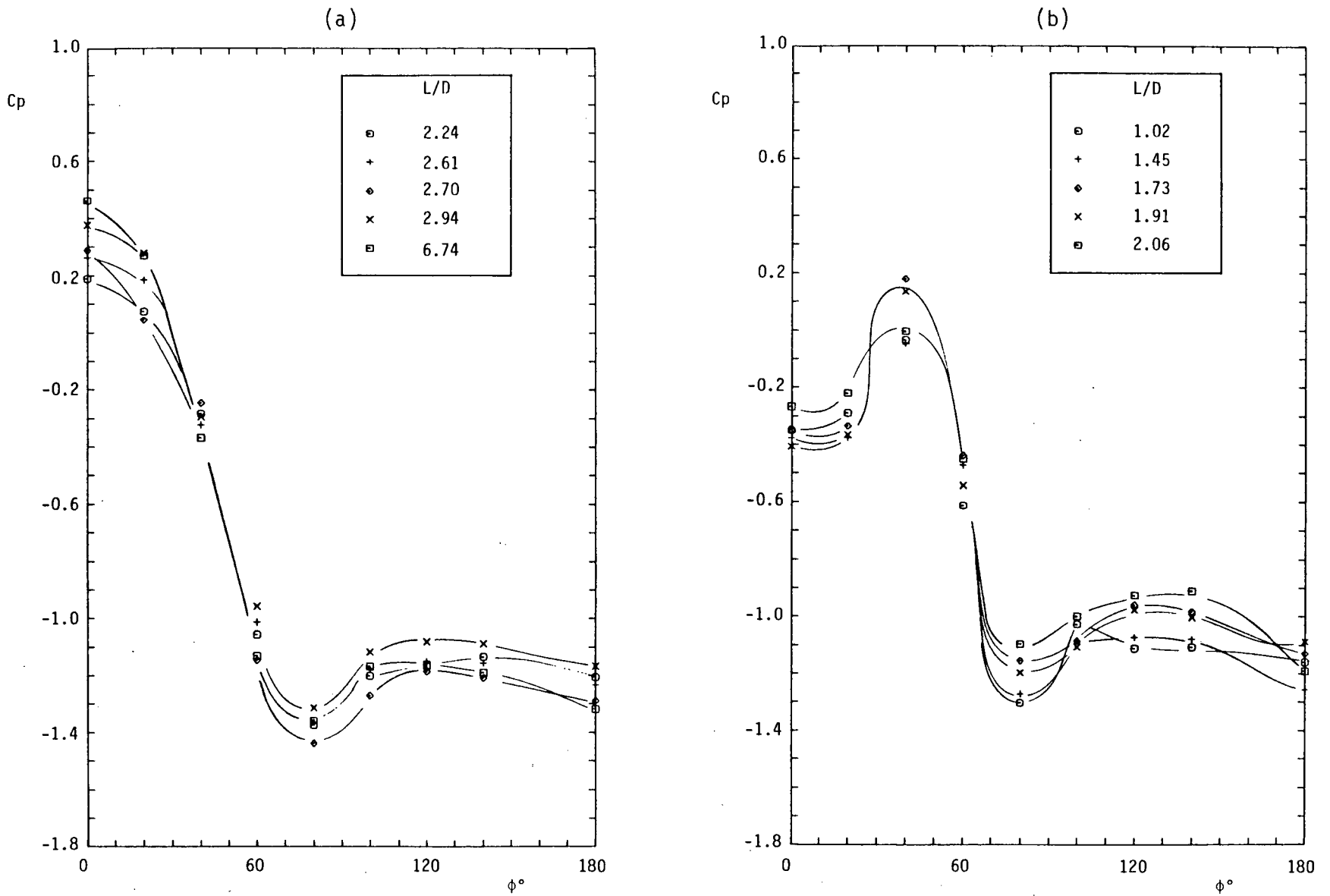

Figure 30 - Pressure distribution around a circular cylinder at Re = 1.0×10^4 with front rod d/D = 0.33. (a) regime A; (b) regime B

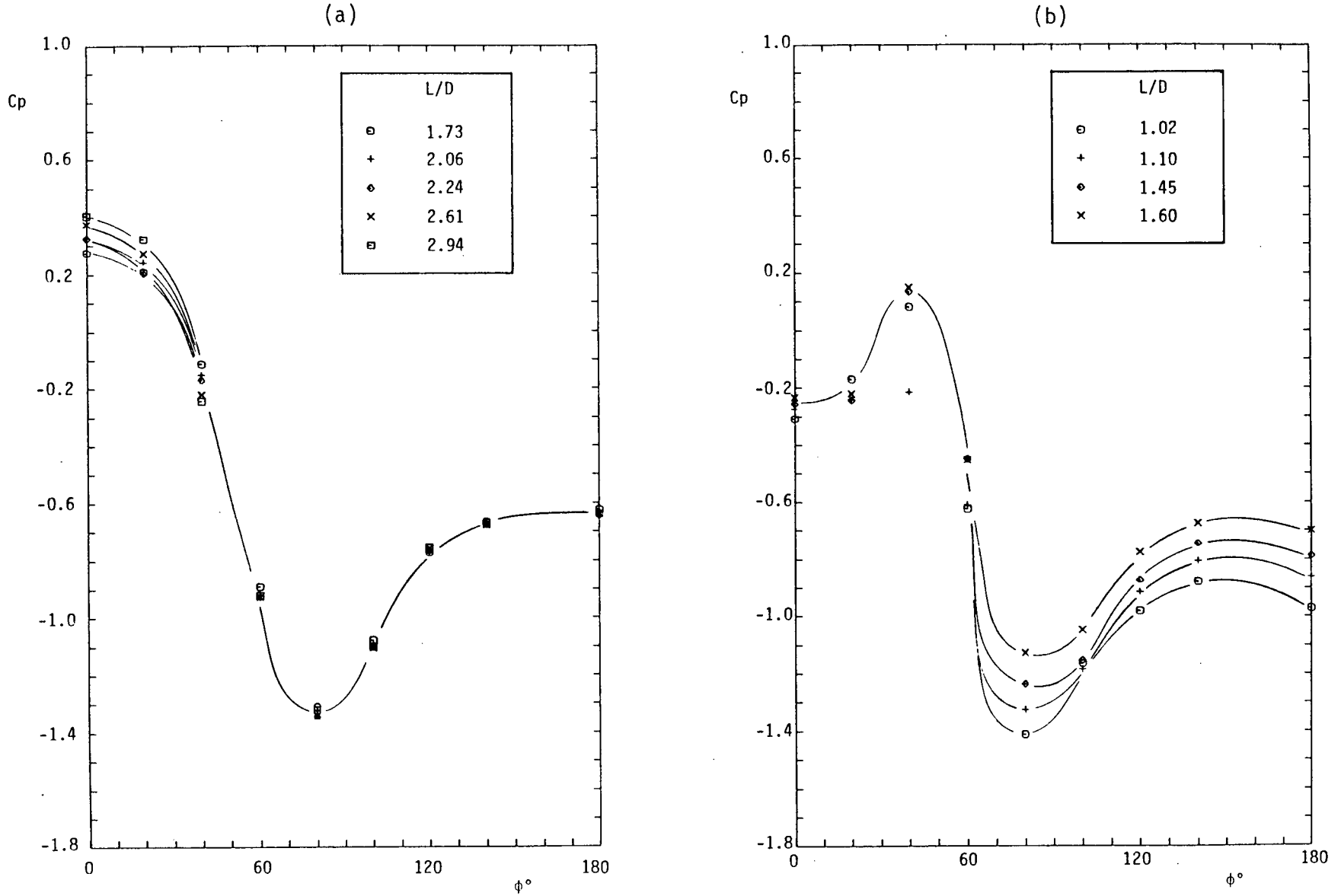

Figure 31 - Pressure distribution around a circular cylinder at Re = 3.3×10^4 with front rod d/D = 0.33. (a) regime A; (b) regime B

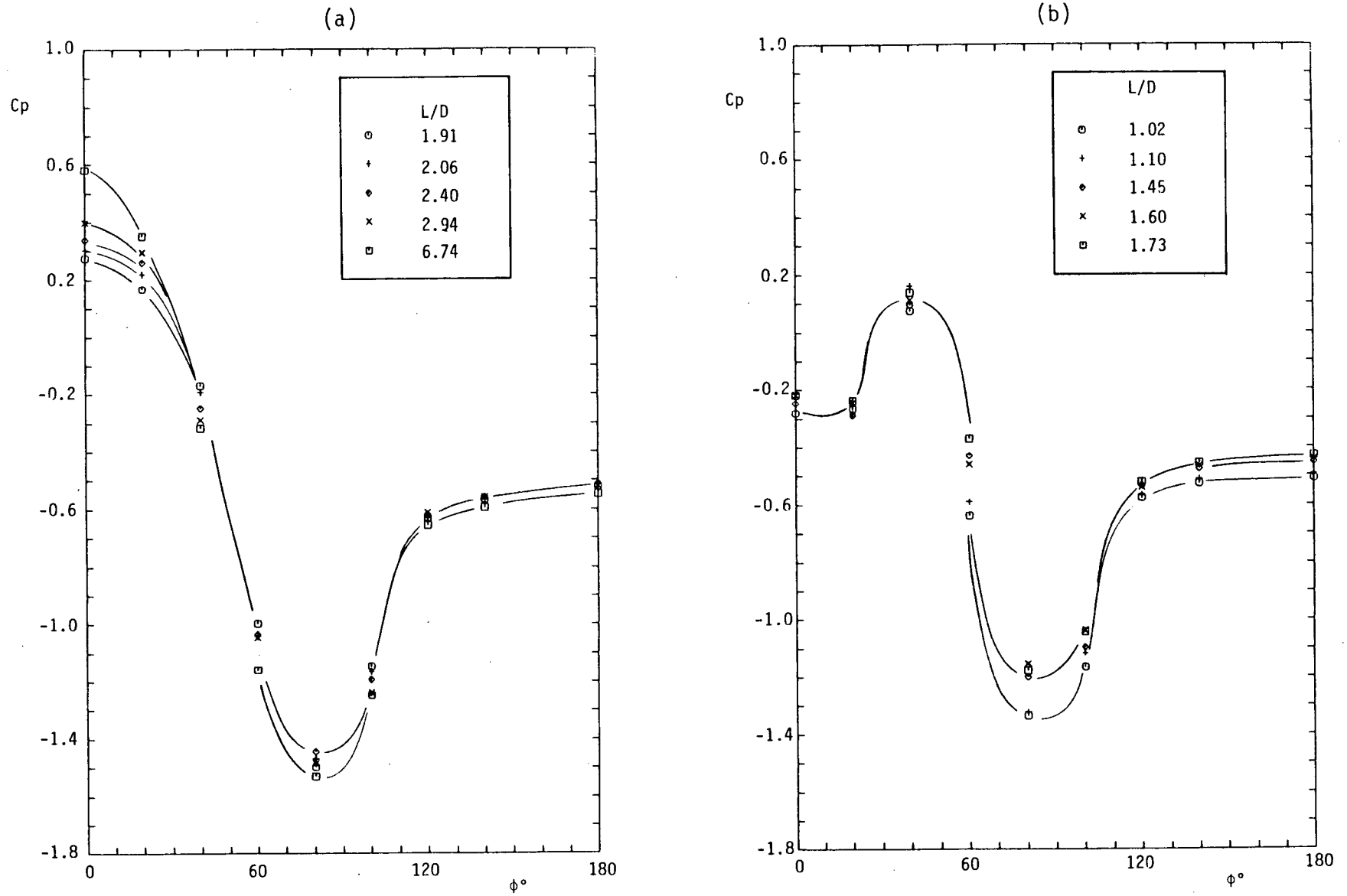

Figure 32 - Pressure distribution around a circular cylinder at Re = 6.5×10^4 with front rod d/D = 0.33.
(a) regime A; (b) regime B

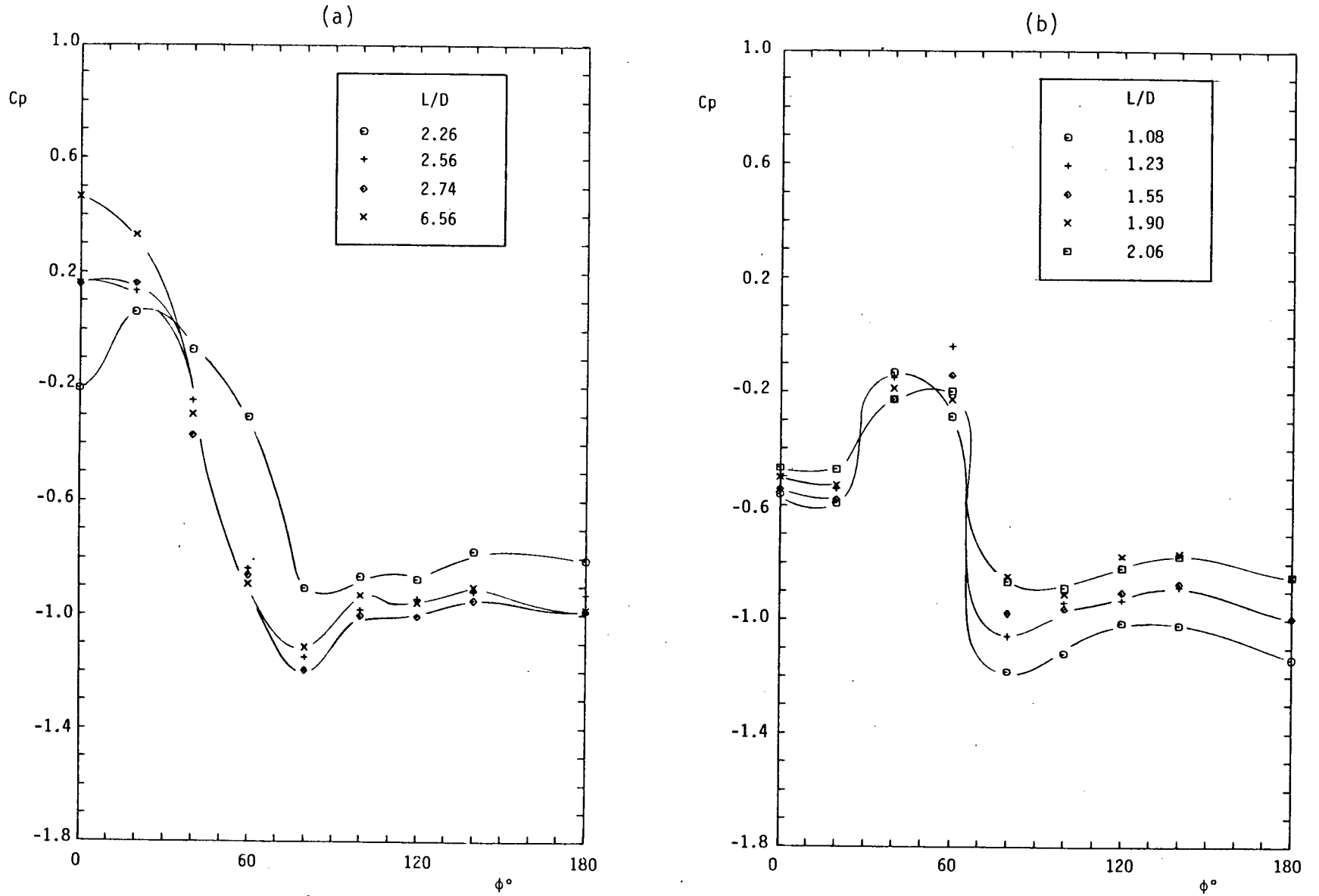

Figure 33 - Pressure distribution around a circular cylinder at Re = 1.0×10^4 with front rod d/D = 0.50. (a) regime A; (b) regime B

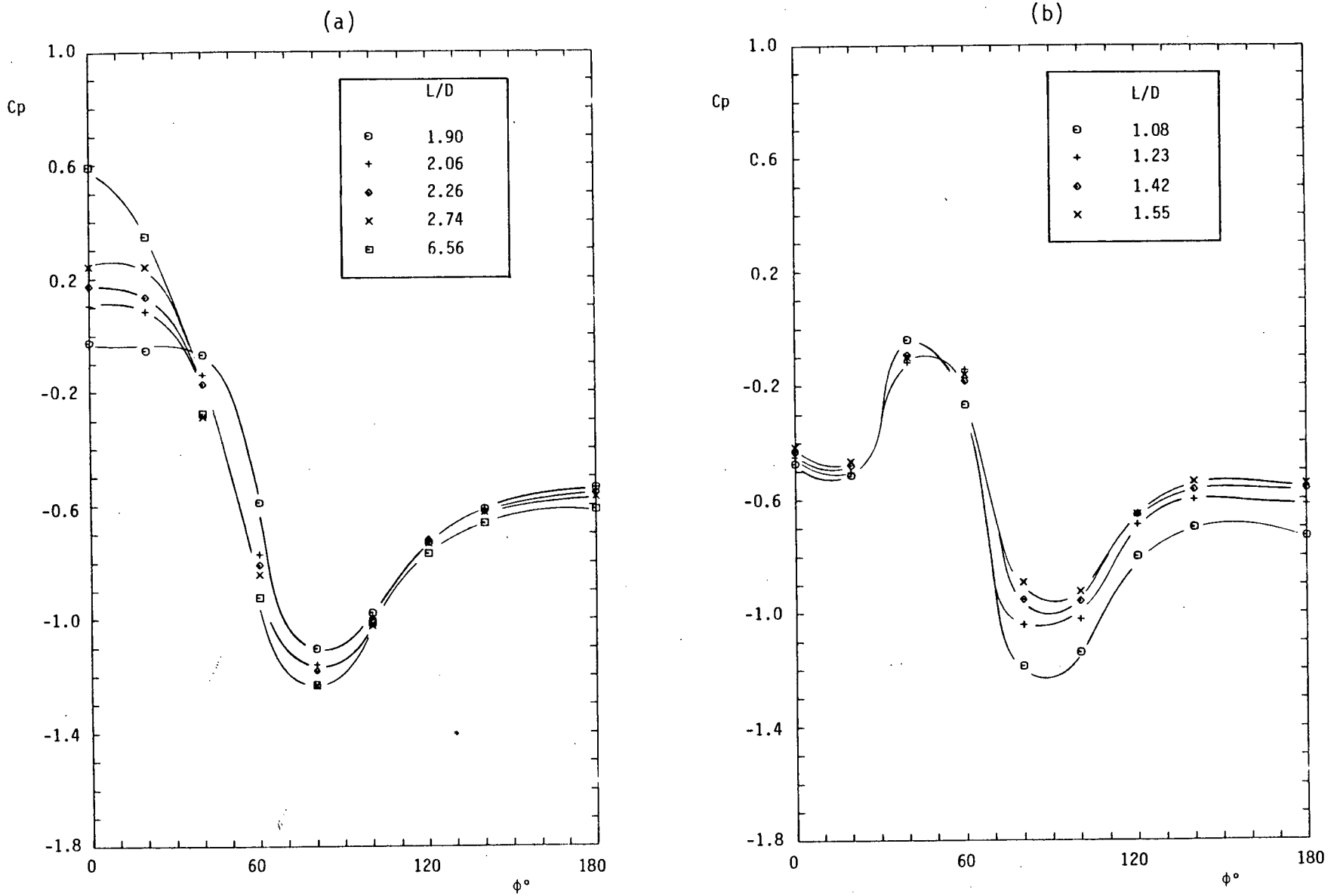

Figure 34 - Pressure distribution around a circular cylinder at Re = 3.3×10^4 with front rod d/D = 0.50. (a) regime A; (b) regime B

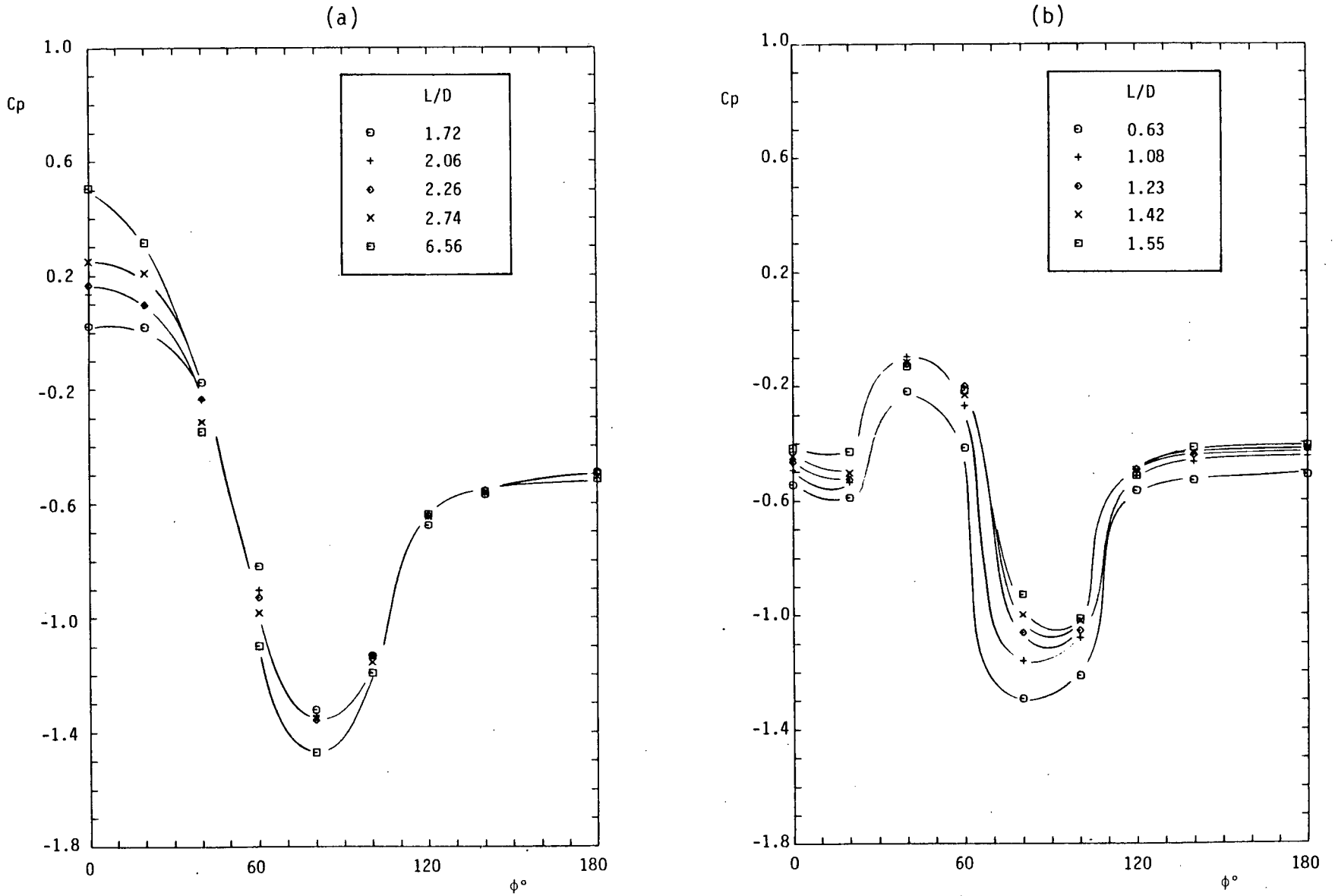

Figure 35 - Pressure distribution around a circular cylinder at Re = 6.5×10^4 with front rod d/D = 0.50. (a) regime A; (b) regime B

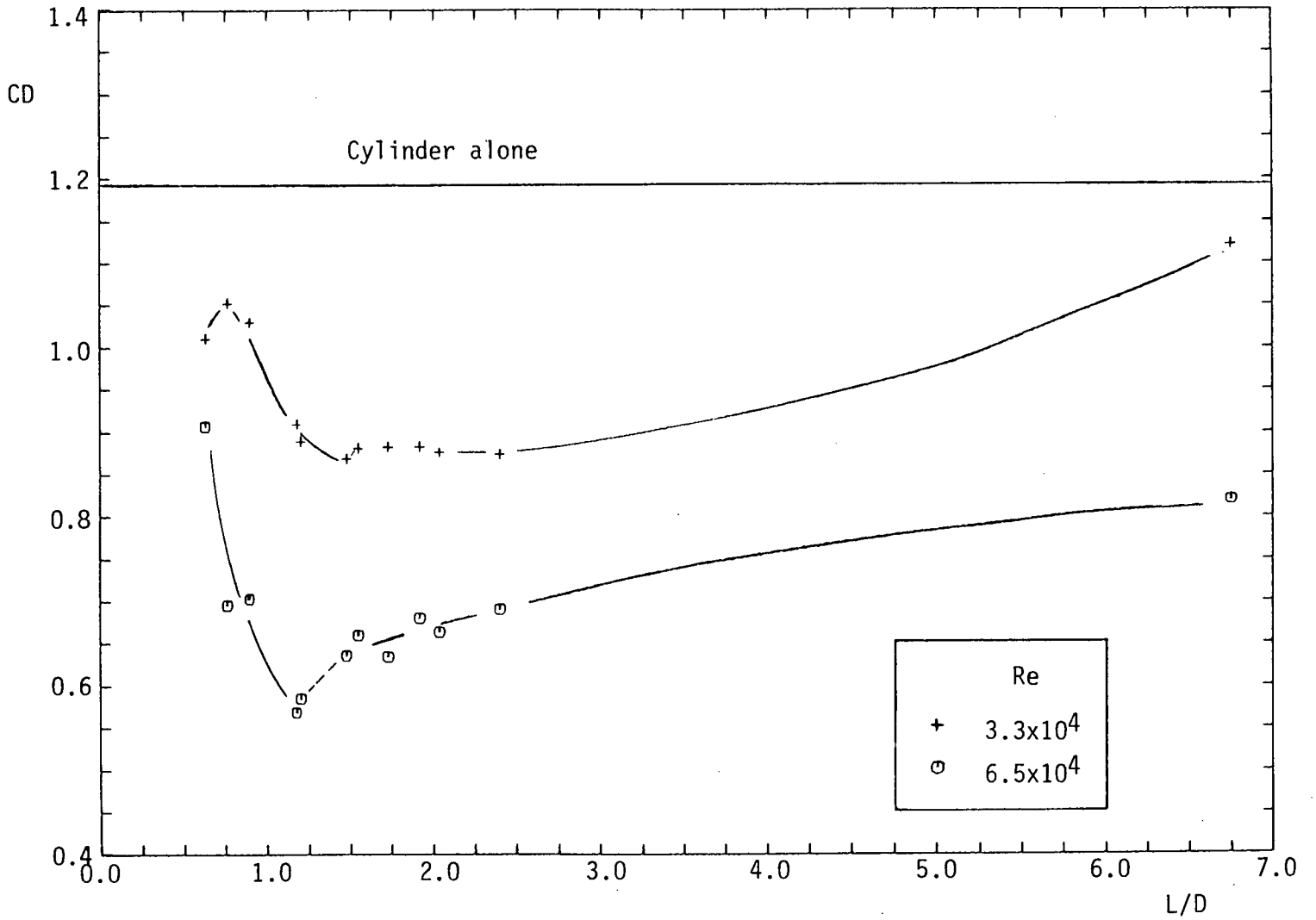

Figure 36 - Overall drag coefficient for cylinder with front rod d/D = 0.17

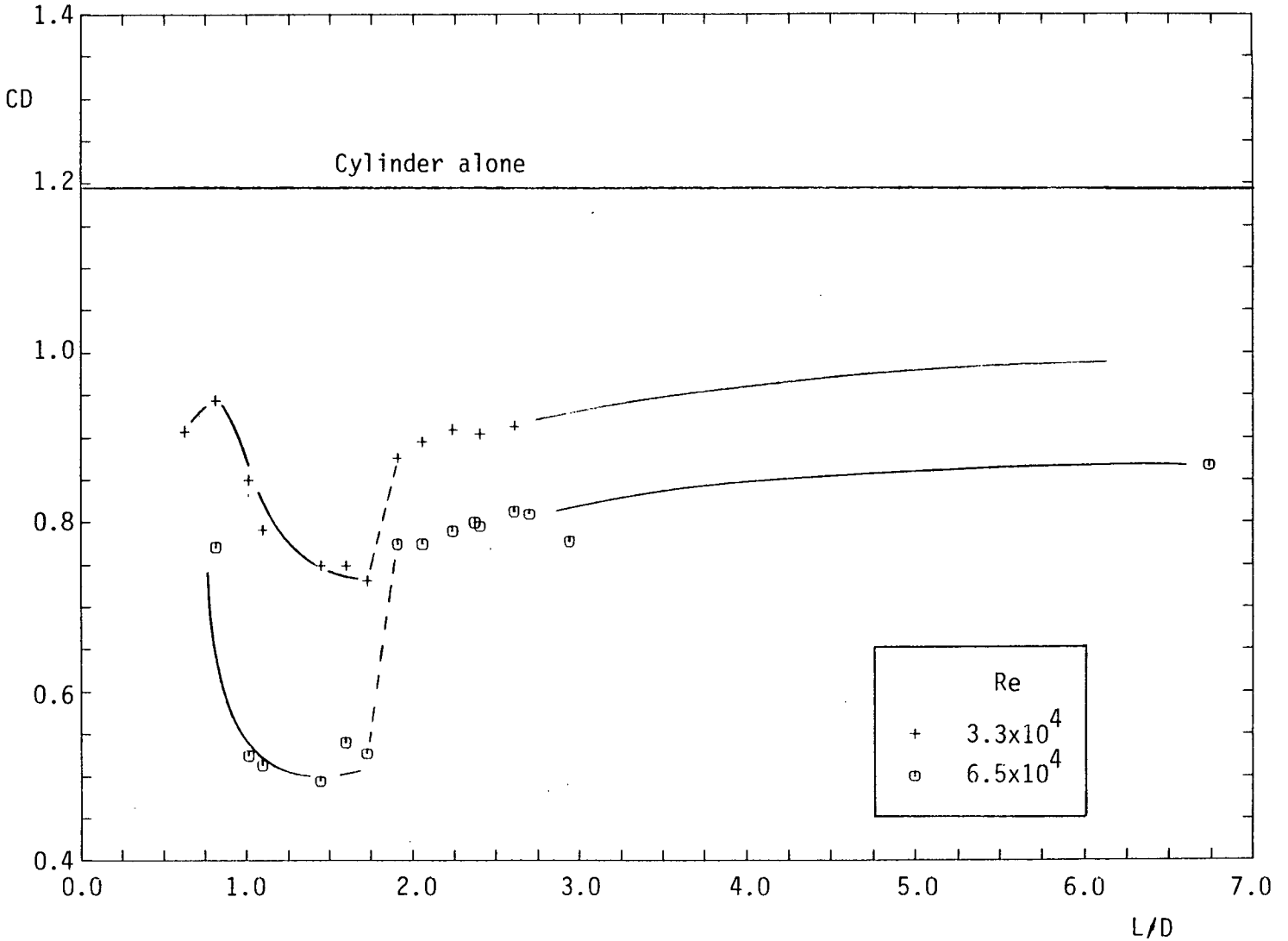

Figure 37 - Overall drag coefficient for cylinder with front rod d/D = 0.33

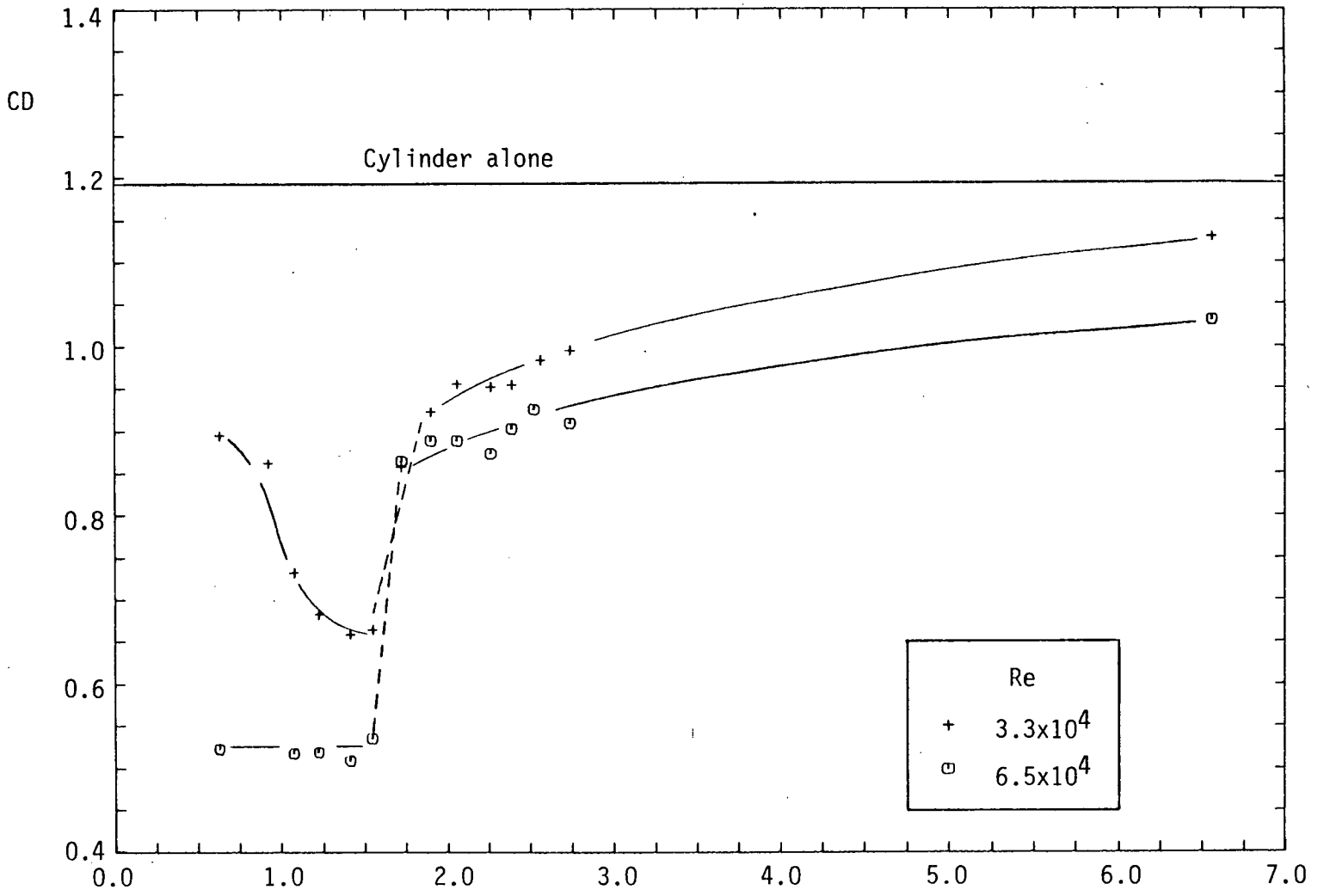

Figure 38 - Overall drag coefficient for cylinder with front rod d/D = 0.50

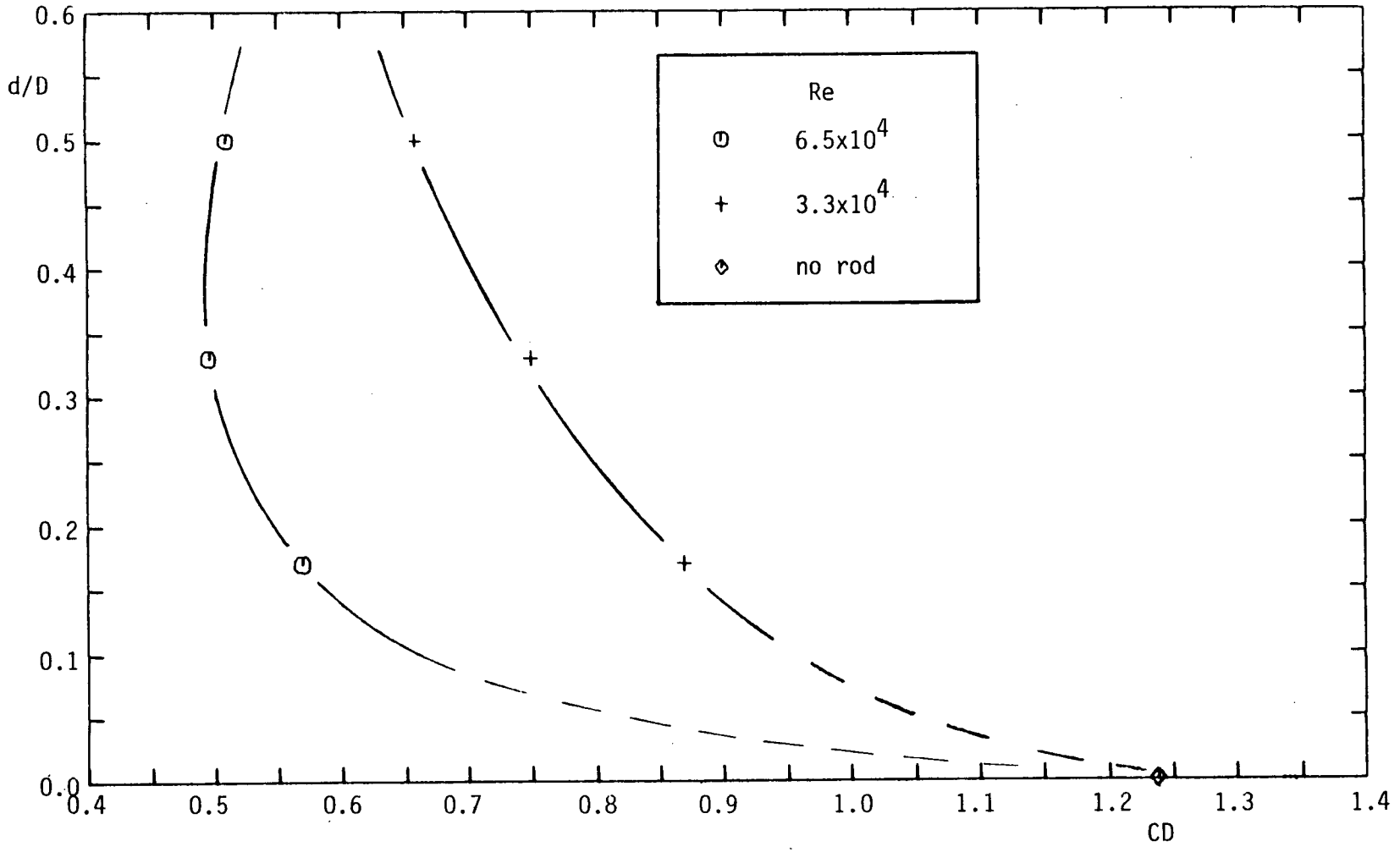

Figure 39 - Rod size for minimum drag (circular cylinder)

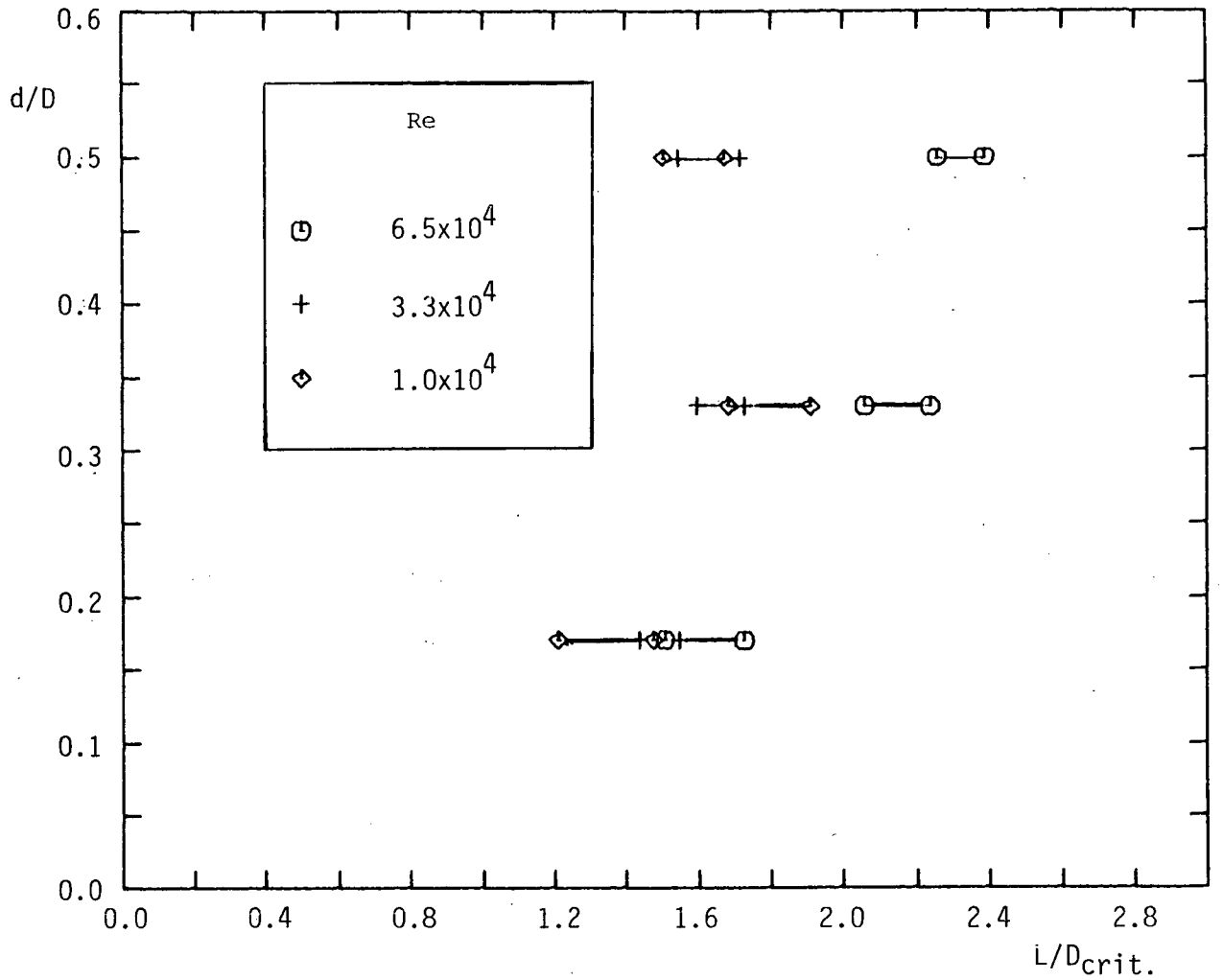

Figure 40 - Critical spacing ranges for different rod sizes and Reynolds numbers (circular cylinder)

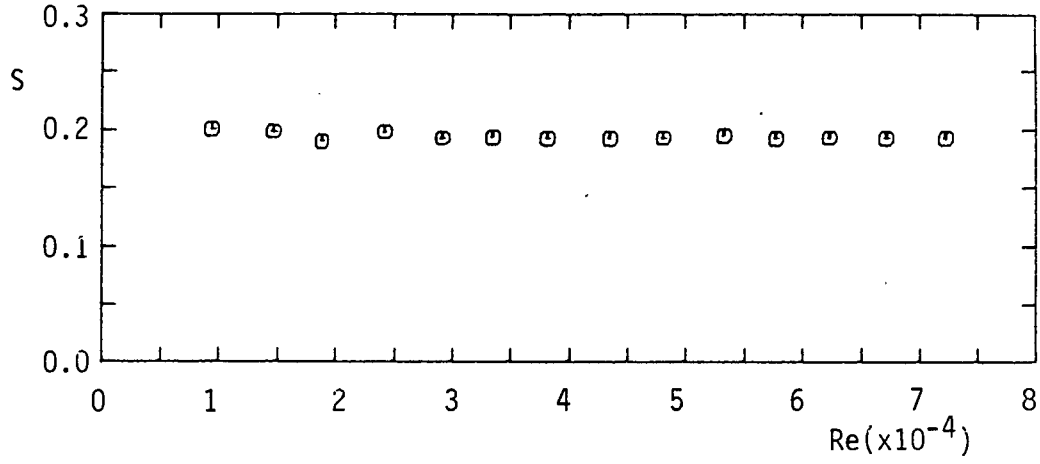

(a)

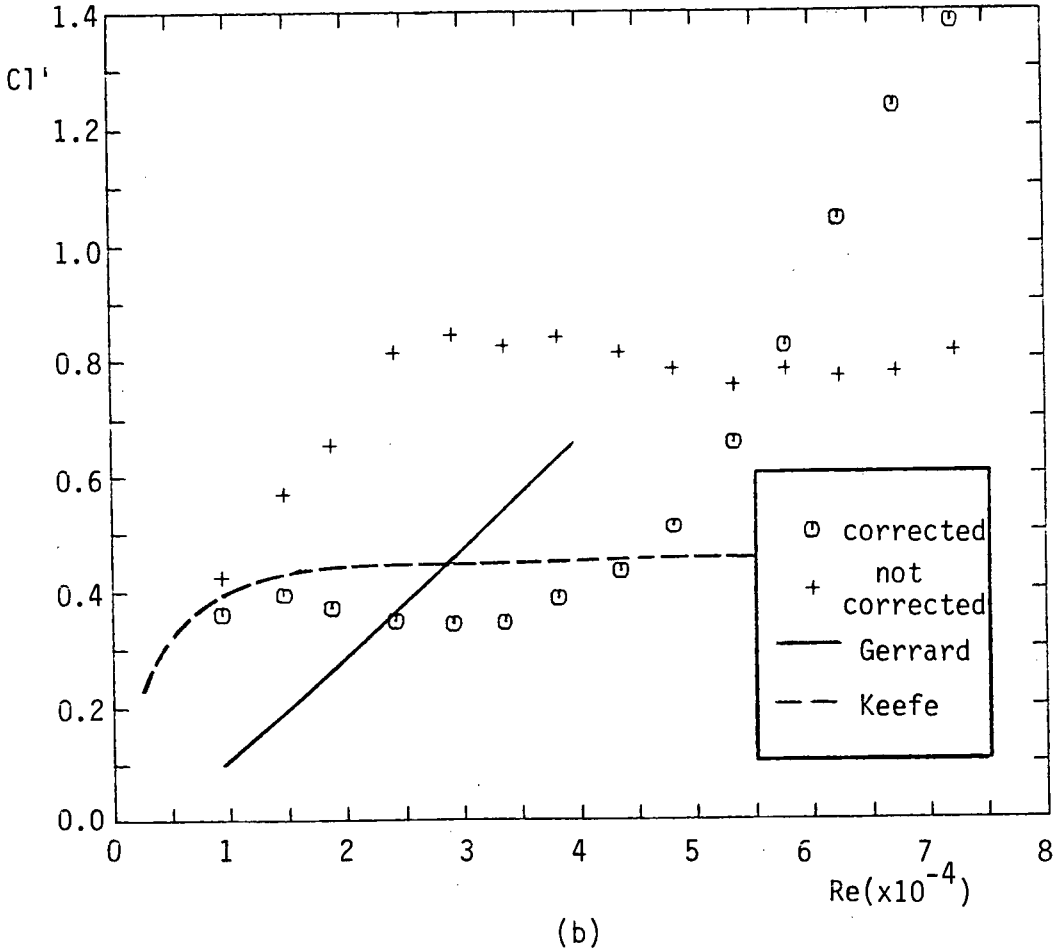

(b)

Figure 41 - Fluctuating side force on a circular cylinder; (a) Strouhal number versus Reynolds number; (b) intensity Cl' versus Reynolds number

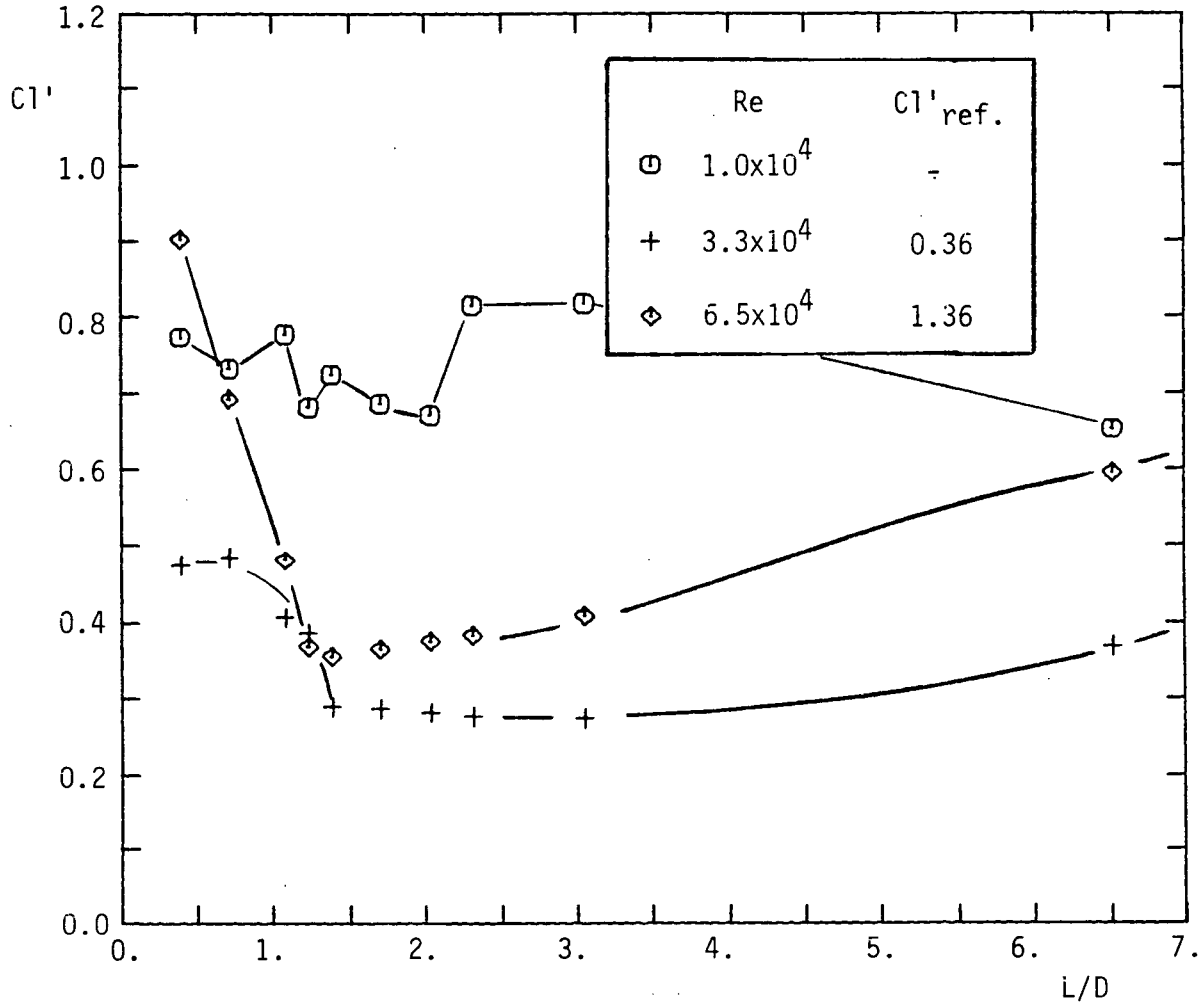

Figure 42 - Fluctuating side force on a circular cylinder with rod d/D = 0.17; $Cl'_{ref.}$ is from Fig.41(b)

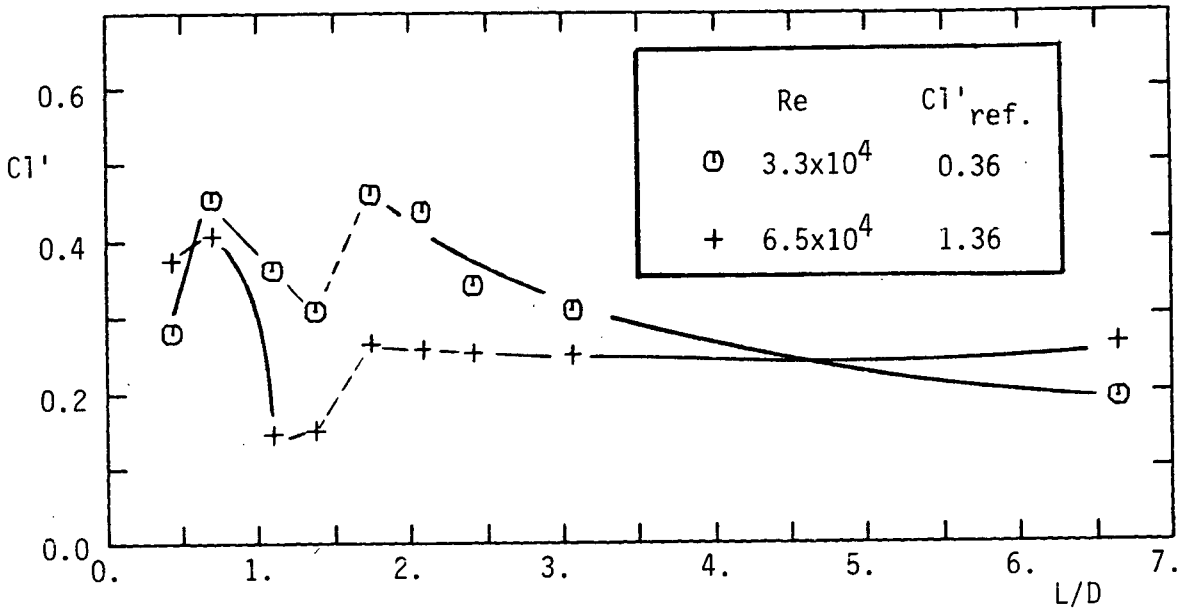

Figure 43 - Fluctuating side force on a circular cylinder with rod d/D = 0.33

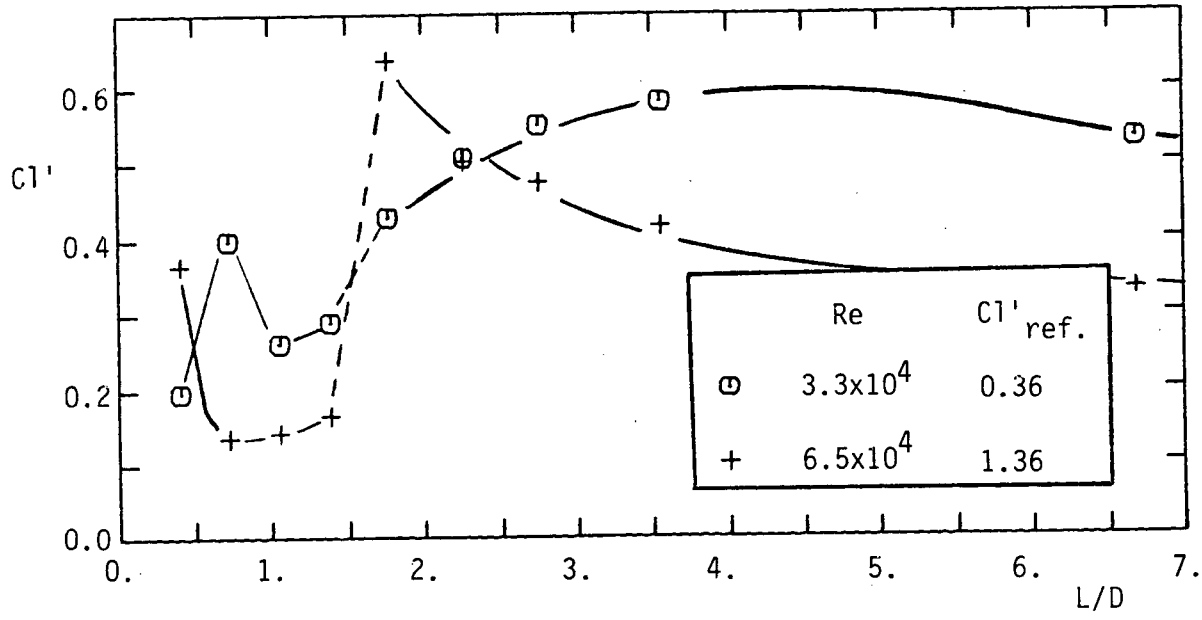

Figure 44 - Fluctuating side force on a circular cylinder with rod d/D = 0.50

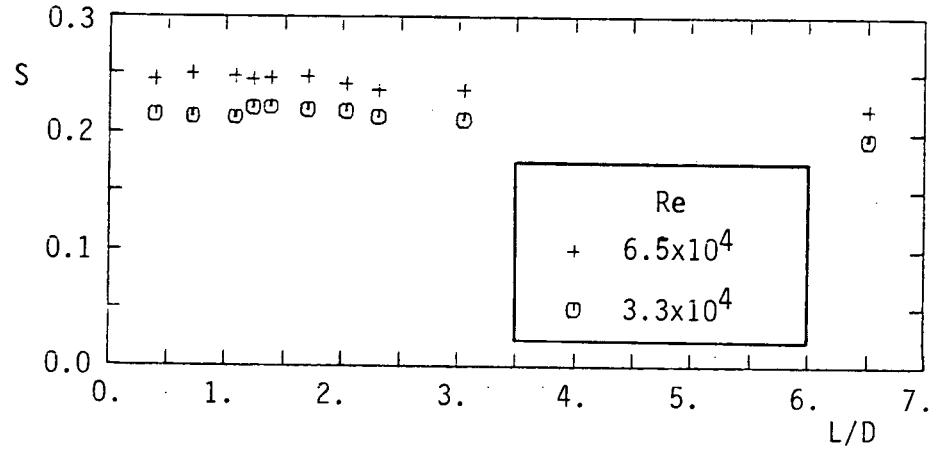

Figure 45 - Strouhal number on a circular cylinder with front rod d/D = 0.17

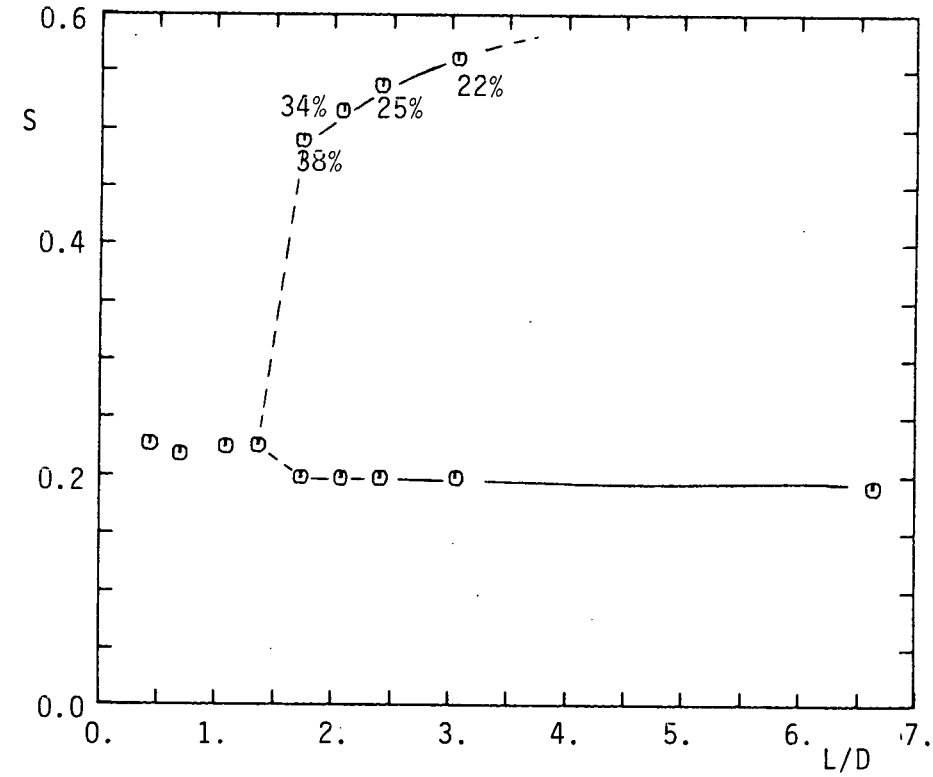

Figure 46 - Strouhal number on a circular cylinder with front rod d/D = 0.33 (Re = 3.3×10^4); percentages shown represent percentage of $(Cl')^2$ due to that frequency

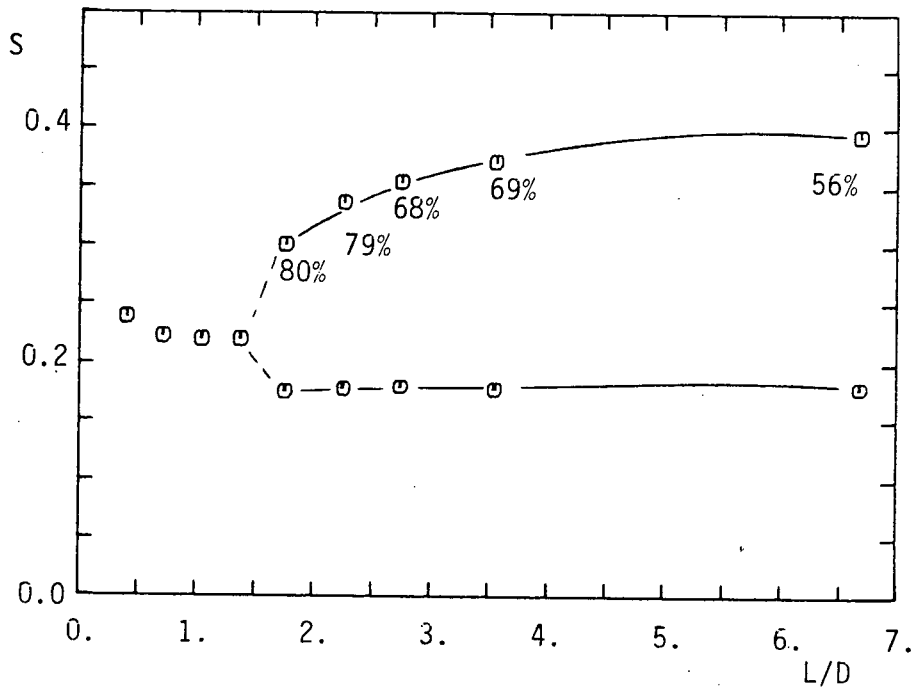

Figure 47 - Strouhal number on a circular cylinder with front rod d/D = 0.50 (Re = 3.3×10^4); percentages shown represent percentage of $(Cl')^2$ due to that frequency

APPENDIX A - PRESSURE TAP LOCATION FOR SIDE FORCE MEASUREMENT

Consider a circular cylinder submitted to a pressure distribution:

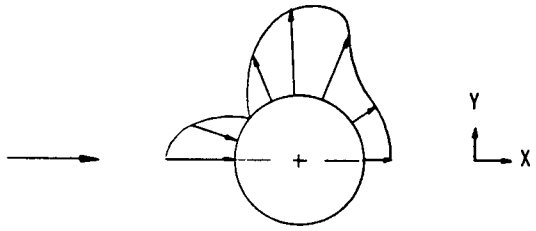

Now divide the Y axis into eight elements and consider each element as being subjected to a uniform pressure equal to the actual pressure at the centre of the element.

The uniformly distributed pressure can be replaced by a point force F:

$$F = p\Delta A = p\Delta y/\sin\theta$$

We are interested only in the side force, or the Y component of F:

$$Fy = F\sin\theta = p\Delta y$$

where Fy is the side force on the element considered. The total side force on the cylinder is the sum over all elements:

$$Fy_T = Fy_1 + Fy_2 + \text{---} + Fy_8$$

$$= p_1\Delta y_1 + p_2\Delta y_2 + \text{---} + p_8\Delta y_8$$

If the elements have the same length, then:

$$Fy_T = (p_1 + p_2 + \text{---} + p_8)\Delta y$$

$$= \frac{(p_1 + p_2 + \text{---} + p_8)}{8} \times 8\Delta y$$

$$= (\text{average pressure}) \times (\text{diameter})$$

If the elements are of equal length, only the average pressure has to be measured to obtain the side force. For elements of the same length, this is the location of pressure taps:

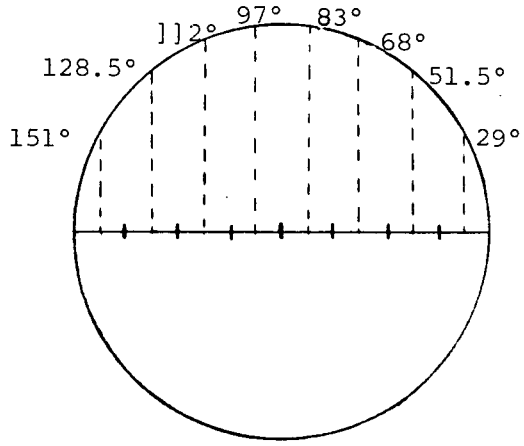

Cl' is calculated in the following way:

$$Cl' = \frac{2 \times \text{manifold pressure(RMS)} \times D}{0.5\rho U_1^2 \times D}$$

The factor 2 is there to include the side force from the other side of the cylinder. By doing that it is assumed that the fluctuating side force is out of phase by 180° from one side to the other. This assumption was not verified here however, but, if anything, Cl' will be overestimated.